

Radiative Corrections to $\gamma\gamma \rightarrow W^+W^-$ in the Electroweak Standard Model

A. DENNER[†]

*Institut für Theoretische Physik, Universität Leipzig
Augustusplatz 10, D-04109 Leipzig, Germany*

S. DITTMAYER[‡]

*Theoretische Physik, Universität Bielefeld
Postfach 100131, D-33501 Bielefeld, Germany*

R. SCHUSTER[§]

*Institut für Theoretische Physik, Universität Würzburg
Am Hubland, D-97074 Würzburg, Germany*

Abstract:

The cross-section for $\gamma\gamma \rightarrow W^+W^-$ with arbitrary polarized photons and W bosons is calculated within the electroweak Standard Model including the complete virtual and soft-photonic $\mathcal{O}(\alpha)$ corrections. We present a detailed numerical discussion of the complete radiative corrections and an analytical investigation of the leading corrections. It turns out that in the on-shell renormalization scheme for fixed M_W no leading corrections associated with the running of α or heavy top-quark and Higgs-boson masses occur. The corrections are typically of the order of 10%. They reach, however, larger values where the lowest-order cross-sections are suppressed.

BI-TP 95/04
WUE-ITP-95-002
March 1995

[†]On leave of absence from Institut für Theoretische Physik, Universität Würzburg, Am Hubland, D-97074 Würzburg, Germany.

[‡]Supported by the Bundesministerium für Forschung und Technologie, Bonn, Germany.

[§]Supported by the Deutsche Forschungsgemeinschaft.

1 Introduction

The $SU(2) \times U(1)$ standard electroweak theory has passed many precision tests during the last years. In particular, measurements of the muon decay constant G_μ , the gauge-boson masses M_W and M_Z , and the decay widths and asymmetries of the Z boson at LEP have provided stringent constraints which are successfully fulfilled by the Standard Model (SM) evaluated at one-loop level. The experimental data favor a value for the top-quark mass which is in accordance with the direct measurements [1] of CDF, $m_t = 176 \pm 16$ GeV, and DØ, $m_t = 199 \pm 30$ GeV. Nevertheless, further precision tests of the SM are required. Up to now, only weak direct experimental information exists on the non-Abelian self-interaction of the gauge bosons [2]. Moreover, no experimental evidence on the mechanism of spontaneous symmetry breaking, which is responsible for mass generation and postulates the existence of the scalar Higgs boson, has been found yet. For such investigations, energies of several hundred GeV or even few TeV are needed, since the sensitivity to deviations from the SM gauge-boson self-interaction grows strongly with energy, and the existence of the Higgs particle can be proven only by direct production. To this end, a “Next Linear Collider” (NLC) for ee , $e\gamma$, and $\gamma\gamma$ collisions was proposed [3] which offers a unique environment for such precision experiments owing to the comparably small background.

A particularly interesting process in $\gamma\gamma$ collisions is $\gamma\gamma \rightarrow W^+W^-$. Its total cross-section approaches a constant of about 80 pb at high energies corresponding to 8×10^6 W pairs for 10 fb^{-1} . This large cross-section is due to the massive t -channel exchange and is drastically reduced by angular cuts. But even for $|\cos\theta| < 0.8$ the cross-section is still 15 and 4 pb at a center-of-mass energy of 500 and 1000 GeV, respectively, and thus much larger as e.g. the one for $e^+e^- \rightarrow W^+W^-$. Hence $\gamma\gamma \rightarrow W^+W^-$ is very well-suited for precision investigations of the SM.

Several features of $\gamma\gamma \rightarrow W^+W^-$ have already been discussed in the literature. Most of the existing works concentrated on tree-level predictions [4], in particular on the influence of anomalous non-Abelian gauge couplings [5, 6, 7]. The process $\gamma\gamma \rightarrow W^+W^-$ depends at tree level both on the triple γWW and the quartic $\gamma\gamma WW$ coupling, and no other vertices are involved in the unitary gauge at lowest order. The sensitivity to the γWW coupling is comparable and complementary to the reactions $e^+e^- \rightarrow W^+W^-$ and $e^-\gamma \rightarrow W^-\nu$: the first involves a mixture of the γWW and the ZWW coupling, the second involves the γWW alone but is less sensitive [6]. Because the sensitivity to the $\gamma\gamma WW$ coupling is much larger than the one in e^+e^- processes, $\gamma\gamma \rightarrow W^+W^-$ is the ideal process to study this coupling [7].

The one-loop diagrams involving a resonant Higgs boson have been calculated in order to study the possible investigation of the Higgs boson via $\gamma\gamma \rightarrow H^* \rightarrow W^+W^-$ [8, 9, 10, 11]. Based on our complete one-loop calculation, we have supplemented these investigations by a discussion of the heavy-Higgs effects in Ref. [12]. As a matter of fact, only the (suppressed) channels of longitudinal W-boson production are sensitive to the Higgs mechanism, but the (dominant) channels of purely transverse W-boson production are extremely insensitive. This insensitivity to the Higgs sector renders $\gamma\gamma \rightarrow W^+W^-$ even more suitable for the investigation of the non-Abelian self couplings.

In this paper, we focus on the complete SM one-loop corrections to $\gamma\gamma \rightarrow W^+W^-$. One reason why these have not been calculated so far is certainly their analytical complexity. We have calculated the numerous Feynman graphs (roughly 300–550 depending on the gauge fixing) by using *Mathematica* [13]. More precisely, we have generated and drawn the Feynman graphs by *FeynArts* [14] and performed three different calculations, one in 't Hooft–Feynman gauge using *FeynCalc* [15] and two in a non-linear gauge with and without using *FeynCalc*. As the final result exhibits a very complicated and untransparent analytical form, we refrain from writing it down in full detail. Instead, we indicate its general structure and present a detailed discussion of the numerical results for the $\mathcal{O}(\alpha)$ (virtual and real soft-photonic) corrections to the polarized as well as unpolarized cross-sections. We restrict the presentation of the analytical results to the lowest-order cross-sections and the most important $\mathcal{O}(\alpha)$ corrections. In particular, we discuss the Higgs resonance, the heavy-Higgs effects, the Coulomb singularity, and the leading effects from light fermions and a heavy top quark.

The paper is organized as follows: After fixing our notation and conventions in Section 2, we consider the lowest-order cross-sections for various polarizations in Section 3. In Section 4 we discuss the evaluation and general features of the radiative corrections and in Section 5 the numerical results.

2 Notation and conventions

We consider the reaction

$$\gamma(k_1, \lambda_1) + \gamma(k_2, \lambda_2) \rightarrow W^+(k_3, \lambda_3) + W^-(k_4, \lambda_4) ,$$

where $\lambda_{1,2} = \pm 1$ and $\lambda_{3,4} = 0, \pm 1$ denote the helicities of the incoming photons and outgoing W bosons, respectively.

In the center-of-mass system (CMS) the momenta read in terms of the beam energy E of the incoming photons and the scattering angle θ

$$\begin{aligned} k_1^\mu &= E(1, 0, 0, -1) , \\ k_2^\mu &= E(1, 0, 0, 1) , \\ k_3^\mu &= E(1, -\beta \sin \theta, 0, -\beta \cos \theta) , \\ k_4^\mu &= E(1, \beta \sin \theta, 0, \beta \cos \theta) , \end{aligned} \tag{1}$$

where $\beta = \sqrt{1 - M_W^2/E^2}$ is the velocity of the W bosons in the CMS. We define the Mandelstam variables

$$\begin{aligned} s &= (k_1 + k_2)^2 = (k_3 + k_4)^2 = 4E^2 , \\ t &= (k_1 - k_3)^2 = (k_2 - k_4)^2 = M_W^2 - \frac{s}{2}(1 - \beta \cos \theta) , \\ u &= (k_1 - k_4)^2 = (k_2 - k_3)^2 = M_W^2 - \frac{s}{2}(1 + \beta \cos \theta) . \end{aligned} \tag{2}$$

In order to calculate polarized cross-sections, we introduce explicit polarization vectors for the photons and W bosons as follows

$$\varepsilon_1^\mu(k_1, \lambda_1 = \pm 1) = \frac{-1}{\sqrt{2}}(0, 1, \mp i, 0) ,$$

$$\begin{aligned}
\varepsilon_2^\mu(k_2, \lambda_2 = \pm 1) &= \frac{1}{\sqrt{2}}(0, 1, \pm i, 0), \\
\varepsilon_3^{*\mu}(k_3, \lambda_3 = \pm 1) &= \frac{-1}{\sqrt{2}}(0, \cos \theta, \pm i, -\sin \theta), \\
\varepsilon_4^{*\mu}(k_4, \lambda_4 = \pm 1) &= \frac{1}{\sqrt{2}}(0, \cos \theta, \mp i, -\sin \theta), \\
\varepsilon_3^{*\mu}(k_3, \lambda_3 = 0) &= \frac{E}{M_W}(\beta, -\sin \theta, 0, -\cos \theta), \\
\varepsilon_4^{*\mu}(k_4, \lambda_4 = 0) &= \frac{E}{M_W}(\beta, \sin \theta, 0, \cos \theta).
\end{aligned} \tag{3}$$

We decompose the amplitude \mathcal{M} into invariant functions F_{ijkl} and standard matrix elements (SME) \mathcal{M}_{ijkl} , which contain the whole information about the boson polarizations. Using the transversality condition for the polarization vectors and Schouten's identity, the amplitude \mathcal{M} can be reduced to

$$\begin{aligned}
\mathcal{M}(\lambda_1, \lambda_2, \lambda_3, \lambda_4, s, t) &= \sum_{i,j=\{0,3,4\}} \sum_{k,l=\{0,1,2\}} F_{ijkl}(s, t) \mathcal{M}_{ijkl}(\lambda_1, \lambda_2, \lambda_3, \lambda_4, s, t) \\
&+ F_{0000}^{(t)}(s, t) \mathcal{M}_{0000}^{(t)}(\lambda_1, \lambda_2, \lambda_3, \lambda_4, s, t) \\
&+ F_{0000}^{(u)}(s, t) \mathcal{M}_{0000}^{(u)}(\lambda_1, \lambda_2, \lambda_3, \lambda_4, s, t)
\end{aligned} \tag{4}$$

with $(i, j = \{3, 4\}, k, l = \{1, 2\})$

$$\mathcal{M}_{ijkl} = (\varepsilon_1 \cdot k_i)(\varepsilon_2 \cdot k_j)(\varepsilon_3^* \cdot k_k)(\varepsilon_4^* \cdot k_l)/s^2, \tag{5}$$

$$\begin{aligned}
\mathcal{M}_{0jkl} &= (\varepsilon_1 \cdot A)(\varepsilon_2 \cdot k_j)(\varepsilon_3^* \cdot k_k)(\varepsilon_4^* \cdot k_l)/s, \\
\mathcal{M}_{i0kl} &= (\varepsilon_1 \cdot k_i)(\varepsilon_2 \cdot A)(\varepsilon_3^* \cdot k_k)(\varepsilon_4^* \cdot k_l)/s, \\
\mathcal{M}_{ij0l} &= (\varepsilon_1 \cdot k_i)(\varepsilon_2 \cdot k_j)(\varepsilon_3^* \cdot A)(\varepsilon_4^* \cdot k_l)/s, \\
\mathcal{M}_{ijk0} &= (\varepsilon_1 \cdot k_i)(\varepsilon_2 \cdot k_j)(\varepsilon_3^* \cdot k_k)(\varepsilon_4^* \cdot A)/s,
\end{aligned} \tag{6}$$

$$\begin{aligned}
\mathcal{M}_{00kl} &= (\varepsilon_1 \cdot \varepsilon_2)(\varepsilon_3^* \cdot k_k)(\varepsilon_4^* \cdot k_l)/s, \\
\mathcal{M}_{0j0l} &= (\varepsilon_1 \cdot \varepsilon_3^*)(\varepsilon_2 \cdot k_j)(\varepsilon_4^* \cdot k_l)/s, \\
\mathcal{M}_{0jk0} &= (\varepsilon_1 \cdot \varepsilon_4^*)(\varepsilon_2 \cdot k_j)(\varepsilon_3^* \cdot k_k)/s, \\
\mathcal{M}_{i00l} &= (\varepsilon_2 \cdot \varepsilon_3^*)(\varepsilon_1 \cdot k_i)(\varepsilon_4^* \cdot k_l)/s, \\
\mathcal{M}_{i0k0} &= (\varepsilon_2 \cdot \varepsilon_4^*)(\varepsilon_1 \cdot k_i)(\varepsilon_3^* \cdot k_k)/s, \\
\mathcal{M}_{ij00} &= (\varepsilon_3^* \cdot \varepsilon_4^*)(\varepsilon_1 \cdot k_i)(\varepsilon_2 \cdot k_j)/s,
\end{aligned} \tag{7}$$

$$\begin{aligned}
\mathcal{M}_{000l} &= (\varepsilon_1 \cdot \varepsilon_2)(\varepsilon_3^* \cdot A)(\varepsilon_4^* \cdot k_l), \\
\mathcal{M}_{00k0} &= (\varepsilon_1 \cdot \varepsilon_2)(\varepsilon_3^* \cdot k_k)(\varepsilon_4^* \cdot A), \\
\mathcal{M}_{0j00} &= (\varepsilon_3^* \cdot \varepsilon_4^*)(\varepsilon_1 \cdot A)(\varepsilon_2 \cdot k_j), \\
\mathcal{M}_{i000} &= (\varepsilon_3^* \cdot \varepsilon_4^*)(\varepsilon_1 \cdot k_i)(\varepsilon_2 \cdot A),
\end{aligned} \tag{8}$$

$$\begin{aligned}
\mathcal{M}_{0000} &= (\varepsilon_1 \cdot \varepsilon_2)(\varepsilon_3^* \cdot \varepsilon_4^*), \\
\mathcal{M}_{0000}^{(t)} &= (\varepsilon_1 \cdot \varepsilon_3^*)(\varepsilon_2 \cdot \varepsilon_4^*), \\
\mathcal{M}_{0000}^{(u)} &= (\varepsilon_1 \cdot \varepsilon_4^*)(\varepsilon_2 \cdot \varepsilon_3^*),
\end{aligned} \tag{9}$$

and

$$A_\mu = \frac{i}{ut - M_W^4} \varepsilon_{\mu\nu\rho\sigma} k_1^\nu k_2^\rho k_3^\sigma, \quad \varepsilon_{0123} = -1. \quad (10)$$

Our choice of polarization vectors for the photons implies

$$\varepsilon_i k_j = 0, \quad i, j = 1, 2, \quad (11)$$

and thus by virtue of momentum conservation

$$\varepsilon_i k_3 = -\varepsilon_i k_4, \quad i = 1, 2. \quad (12)$$

We use this relation to eliminate all SME involving $\varepsilon_1 k_4$ and $\varepsilon_2 k_3$. This reduces the 83 SME defined in (5) – (9) to 38 for the process under consideration.

As a consequence of CP invariance and Bose symmetry only the sum of each SME and the one with $(\varepsilon_1, k_1, \varepsilon_3, k_3)$ and $(\varepsilon_2, k_2, \varepsilon_4, k_4)$ interchanged occurs. For instance, \mathcal{M}_{0401} only appears in the combination $\mathcal{M}_{0401} + \mathcal{M}_{3020}$ in the expansion of \mathcal{M} in (4). This leaves 22 independent SME.

In four dimensions, the matrix elements $\mathcal{M}_{0000}^{(t)}$ and $\mathcal{M}_{0000}^{(u)}$ are not linearly independent from the set of all \mathcal{M}_{ijkl} and can be reduced to linear combinations of the other matrix elements using the identities

$$\delta_{\varepsilon_2 \varepsilon_4^* k_1 k_2 k_3}^{\varepsilon_1 \varepsilon_3^* k_1 k_2 k_3} = \delta_{\varepsilon_2 \varepsilon_3^* k_1 k_2 k_3}^{\varepsilon_1 \varepsilon_4^* k_1 k_2 k_3} = 0 \quad (13)$$

involving the Gram determinant

$$\delta_{q_1 \dots q_n}^{p_1 \dots p_n} = \begin{vmatrix} p_1 \cdot q_1 & \dots & p_1 \cdot q_n \\ \vdots & \ddots & \vdots \\ p_n \cdot q_1 & \dots & p_n \cdot q_n \end{vmatrix}. \quad (14)$$

Nevertheless, we keep $\mathcal{M}_{0000}^{(t)}$ and $\mathcal{M}_{0000}^{(u)}$ for convenience.

Bose symmetry implies that the amplitude \mathcal{M} is invariant under the interchange $(k_1, \varepsilon_1) \leftrightarrow (k_2, \varepsilon_2)$. Since many diagrams can be related to others by this transformation, it is useful to introduce a second set of SME which is obtained from (5)–(9) by this interchange. Of course, this second set of SME can be expressed by the original set.

Besides Bose symmetry also CP is an exact symmetry, since we use a unit quark-mixing matrix.¹ The helicity amplitudes for fixed polarization configurations are related as follows

$$\begin{aligned} \mathcal{M}_{\lambda_1 \lambda_2 \lambda_3 \lambda_4}(s, t, u) &= \mathcal{M}_{\lambda_2 \lambda_1 \lambda_3 \lambda_4}(s, u, t) && \text{(Bose)} \\ \mathcal{M}_{\lambda_1 \lambda_2 \lambda_3 \lambda_4}(s, t, u) &= \mathcal{M}_{-\lambda_1 -\lambda_2 -\lambda_4 -\lambda_3}(s, u, t) && \text{(CP)} \\ \mathcal{M}_{\lambda_1 \lambda_2 \lambda_3 \lambda_4}(s, t, u) &= \mathcal{M}_{-\lambda_2 -\lambda_1 -\lambda_4 -\lambda_3}(s, t, u) && \text{(Bose+CP)}. \end{aligned} \quad (15)$$

In the following, we only consider the sum of the two transverse W polarizations. Therefore we indicate the polarizations of the external particles by four labels, the first pair corresponding to the photons, and the second pair to the W bosons. The labels +, –

¹For a non-trivial quark-mixing matrix, CP would be violated in the considered process first at two-loop level.

represent right-handed and left-handed photons, respectively, L stands for longitudinal, and T for the sum of the two transverse W polarizations.

The combination of Bose and CP symmetry leads to the following relations between the differential cross-sections with equal photon helicities

$$\begin{aligned} \left(\frac{d\sigma}{d\Omega}\right)_{--\text{TT}} &= \left(\frac{d\sigma}{d\Omega}\right)_{++\text{TT}} , \\ \left(\frac{d\sigma}{d\Omega}\right)_{--\text{LL}} &= \left(\frac{d\sigma}{d\Omega}\right)_{++\text{LL}} , \\ \left(\frac{d\sigma}{d\Omega}\right)_{--(\text{LT}+\text{TL})} &= \left(\frac{d\sigma}{d\Omega}\right)_{++(\text{LT}+\text{TL})} . \end{aligned} \quad (16)$$

Moreover, Bose symmetry implies that all cross-sections in (16) are forward-backward symmetric. For different photon helicities Bose symmetry leads to

$$\begin{aligned} \left(\frac{d\sigma}{d\Omega}\right)_{-+\text{TT}}(s, t, u) &= \left(\frac{d\sigma}{d\Omega}\right)_{+-\text{TT}}(s, u, t) , \\ \left(\frac{d\sigma}{d\Omega}\right)_{-+\text{LL}}(s, t, u) &= \left(\frac{d\sigma}{d\Omega}\right)_{+-\text{LL}}(s, u, t) , \\ \left(\frac{d\sigma}{d\Omega}\right)_{-+(\text{LT}+\text{TL})}(s, t, u) &= \left(\frac{d\sigma}{d\Omega}\right)_{+-(\text{LT}+\text{TL})}(s, u, t) , \end{aligned} \quad (17)$$

whereas Bose+CP does not yield further relations.

C and P symmetry are only violated by the fermionic loop corrections, but hold in lowest order and for the bosonic loop corrections. We indicate these restricted symmetries by a modified equality sign

$$\begin{aligned} \mathcal{M}_{\lambda_1\lambda_2\lambda_3\lambda_4}(s, t, u) &\stackrel{\bar{P}}{=} \mathcal{M}_{-\lambda_1-\lambda_2-\lambda_3-\lambda_4}(s, t, u) , \\ \mathcal{M}_{\lambda_1\lambda_2\lambda_3\lambda_4}(s, t, u) &\stackrel{\bar{C}}{=} \mathcal{M}_{\lambda_1\lambda_2\lambda_4\lambda_3}(s, u, t) . \end{aligned} \quad (18)$$

P invariance then implies for the differential cross-sections

$$\begin{aligned} \left(\frac{d\sigma}{d\Omega}\right)_{-+\text{TT}} &\stackrel{\bar{P}}{=} \left(\frac{d\sigma}{d\Omega}\right)_{+-\text{TT}} , \\ \left(\frac{d\sigma}{d\Omega}\right)_{-+\text{LL}} &\stackrel{\bar{P}}{=} \left(\frac{d\sigma}{d\Omega}\right)_{+-\text{LL}} , \\ \left(\frac{d\sigma}{d\Omega}\right)_{-+(\text{LT}+\text{TL})} &\stackrel{\bar{P}}{=} \left(\frac{d\sigma}{d\Omega}\right)_{+-(\text{LT}+\text{TL})} . \end{aligned} \quad (19)$$

In combination with (17) this means that the forward-backward asymmetries of the differential cross-sections for unequal photon helicities are entirely due to fermionic corrections.

We perform the calculation both in 't Hooft-Feynman (tHF) gauge and in a gauge with the following non-linear (NL) gauge-fixing term [16]

$$\begin{aligned} \mathcal{L}_{\text{GF}} &= - \left| \partial^\mu W_\mu^+ + ie(A^\mu - \frac{c_W}{s_W} Z^\mu) W_\mu^+ - iM_W \phi^+ \right|^2 \\ &\quad - \frac{1}{2} (\partial^\mu Z_\mu - M_Z \chi)^2 - \frac{1}{2} (\partial^\mu A_\mu)^2 , \end{aligned} \quad (20)$$

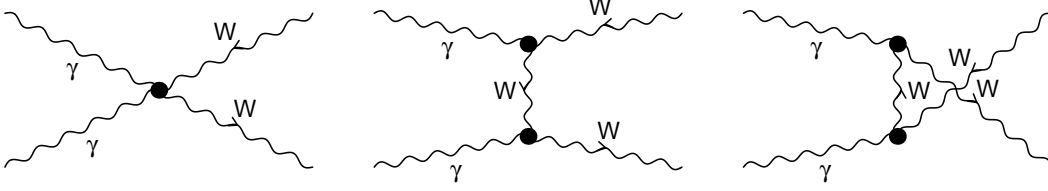


Figure 1: Lowest-order diagrams for $\gamma\gamma \rightarrow W^+W^-$ in NL gauge

with the conventions of Ref. [17] for the fields. In particular, ϕ^\pm and χ denote the charged and neutral would-be-Goldstone fields, respectively. In this NL gauge the $\phi^\pm W^\mp A$ vertices vanish. This reduces the number of Feynman graphs in comparison to the tHF gauge considerably.

3 Lowest-order cross-section

In NL gauge, only the three diagrams of Fig. 1 contribute to the lowest-order amplitude. In tHF gauge two additional diagrams exist which involve internal ϕ fields. Evaluation of the tree diagrams in either gauge yields the Born amplitude

$$\mathcal{M}_{\text{Born}} = 8\pi\alpha \left\{ \frac{s}{M_W^2 - t} \mathcal{M}_{0,t} + \frac{s}{M_W^2 - u} \mathcal{M}_{0,u} - \mathcal{M}_{0000} \right\}, \quad (21)$$

where

$$\begin{aligned} \mathcal{M}_{0,t} &= 2\mathcal{M}_{0012} + 2\mathcal{M}_{3400} - 2\mathcal{M}_{0401} - 2\mathcal{M}_{3020} + 2\mathcal{M}_{0410} + 2\mathcal{M}_{3002} + \mathcal{M}_{0000}^{(t)}, \\ \mathcal{M}_{0,u} &= 2\mathcal{M}_{0021} + 2\mathcal{M}_{4300} - 2\mathcal{M}_{0310} - 2\mathcal{M}_{4002} + 2\mathcal{M}_{0301} + 2\mathcal{M}_{4020} + \mathcal{M}_{0000}^{(u)}. \end{aligned} \quad (22)$$

The lowest-order matrix element vanishes for the helicities $(\lambda_1, \lambda_2, \lambda_3, \lambda_4) = (\pm, \pm, 0, \pm), (\pm, \pm, \pm, 0), (\pm, \pm, 0, \mp), (\pm, \pm, \mp, 0), (\pm, \pm, \pm, \mp), (\pm, \pm, \mp, \pm)$.

The differential Born cross-section [6, 7] is obtained as

$$\left(\frac{d\sigma}{d\Omega} \right)^{\text{Born}} = \frac{\beta}{64\pi^2 s} \sum_{\lambda_1 \lambda_2 \lambda_3 \lambda_4} \frac{1}{4} (1 + \lambda_1 P_1^\gamma) (1 + \lambda_2 P_2^\gamma) |\mathcal{M}_{\text{Born}}|^2, \quad (23)$$

where $P_{1,2}^\gamma$ denote the degrees of photon-beam polarization and the sum over λ_3, λ_4 include the desired W polarizations.

We list the differential cross-sections for several helicity configurations:

$$\begin{aligned} \left(\frac{d\sigma}{d\Omega} \right)_{\pm\pm\text{TT}}^{\text{Born}} &= \frac{\alpha^2 \beta s (2M_W^4 - 4M_W^2 s + s^2)}{(M_W^2 - t)^2 (M_W^2 - u)^2}, \\ \left(\frac{d\sigma}{d\Omega} \right)_{\pm\pm\text{LL}}^{\text{Born}} &= \frac{\alpha^2 \beta M_W^4 s}{(M_W^2 - t)^2 (M_W^2 - u)^2}, \\ \left(\frac{d\sigma}{d\Omega} \right)_{\pm\pm(\text{LT}+\text{TL})}^{\text{Born}} &= 0, \end{aligned}$$

$$\begin{aligned}
\left(\frac{d\sigma}{d\Omega}\right)_{\pm\mp\text{TT}}^{\text{Born}} &= \frac{\alpha^2\beta s^3}{(M_{\text{W}}^2 - t)^2(M_{\text{W}}^2 - u)^2} \left\{ 2 \frac{(16M_{\text{W}}^4 + s^2)(ut - M_{\text{W}}^4)^2}{s^6\beta^4} + \frac{(t - u)^2}{s^2\beta^2} \right\}, \\
\left(\frac{d\sigma}{d\Omega}\right)_{\pm\mp\text{LL}}^{\text{Born}} &= \frac{\alpha^2(4M_{\text{W}}^2 + s)^2(M_{\text{W}}^4 - tu)^2}{\beta^3 s^3 (M_{\text{W}}^2 - t)^2 (M_{\text{W}}^2 - u)^2}, \\
\left(\frac{d\sigma}{d\Omega}\right)_{\pm\mp(\text{LT}+\text{TL})}^{\text{Born}} &= \frac{16\alpha^2 M_{\text{W}}^2 (2M_{\text{W}}^4 - t^2 - u^2)(M_{\text{W}}^4 - tu)}{\beta^3 s^2 (M_{\text{W}}^2 - t)^2 (M_{\text{W}}^2 - u)^2}. \tag{24}
\end{aligned}$$

These results can be reconstructed from equation (5) in Ref. [7] or from equation (4.5) in Ref. [6].

Adding up the single contributions, we get for the unpolarized differential cross-section²

$$\begin{aligned}
\left(\frac{d\sigma}{d\Omega}\right)_{\text{unpol}}^{\text{Born}} &= \frac{3\alpha^2\beta}{2s} \left\{ 1 - \frac{2s^2}{(M_{\text{W}}^2 - t)(M_{\text{W}}^2 - u)} \left(\frac{2}{3} + \frac{M_{\text{W}}^2}{s} \right) \right. \\
&\quad \left. + \frac{2s^4}{(M_{\text{W}}^2 - t)^2(M_{\text{W}}^2 - u)^2} \left(\frac{1}{3} + \frac{M_{\text{W}}^4}{s^2} \right) \right\}. \tag{25}
\end{aligned}$$

Integration over $\theta_{\text{cut}} \leq \theta \leq \pi - \theta_{\text{cut}}$ yields:

$$\begin{aligned}
\sigma_{\pm\pm\text{TT}}^{\text{Born}} &= \frac{16\pi\alpha^2}{s} \frac{s^2 - 4M_{\text{W}}^2 s + 2M_{\text{W}}^4}{s^2} \left\{ \log \left(\frac{1 + \beta \cos \theta_{\text{cut}}}{1 - \beta \cos \theta_{\text{cut}}} \right) + \frac{2\beta \cos \theta_{\text{cut}}}{1 - \beta^2 \cos^2 \theta_{\text{cut}}} \right\}, \\
\sigma_{\pm\pm\text{LL}}^{\text{Born}} &= \frac{16\pi\alpha^2}{s} \frac{M_{\text{W}}^4}{s^2} \left\{ \log \left(\frac{1 + \beta \cos \theta_{\text{cut}}}{1 - \beta \cos \theta_{\text{cut}}} \right) + \frac{2\beta \cos \theta_{\text{cut}}}{1 - \beta^2 \cos^2 \theta_{\text{cut}}} \right\}, \\
\sigma_{\pm\mp\text{TT}}^{\text{Born}} &= \frac{8\pi\alpha^2}{s\beta^4} \left\{ \frac{s^2 + 16M_{\text{W}}^4}{s^2} \beta \cos \theta_{\text{cut}} \right. \\
&\quad \left. - 2 \frac{s^4 - 2M_{\text{W}}^2 s^3 - 2M_{\text{W}}^4 s^2 + 32M_{\text{W}}^6 s - 32M_{\text{W}}^8}{s^4} \log \left(\frac{1 + \beta \cos \theta_{\text{cut}}}{1 - \beta \cos \theta_{\text{cut}}} \right) \right. \\
&\quad \left. + 4 \frac{s^4 - 4M_{\text{W}}^2 s^3 + 2M_{\text{W}}^4 s^2 + 32M_{\text{W}}^8}{s^4} \frac{\beta \cos \theta_{\text{cut}}}{1 - \beta^2 \cos^2 \theta_{\text{cut}}} \right\}, \\
\sigma_{\pm\mp\text{LL}}^{\text{Born}} &= \frac{4\pi\alpha^2}{s\beta^4} \frac{(4M_{\text{W}}^2 + s)^2}{s^2} \left\{ \beta \cos \theta_{\text{cut}} - 4 \frac{M_{\text{W}}^2 (s - M_{\text{W}}^2)}{s^2} \log \left(\frac{1 + \beta \cos \theta_{\text{cut}}}{1 - \beta \cos \theta_{\text{cut}}} \right) \right. \\
&\quad \left. + \frac{8M_{\text{W}}^4}{s^2} \frac{\beta \cos \theta_{\text{cut}}}{1 - \beta^2 \cos^2 \theta_{\text{cut}}} \right\}, \\
\sigma_{\pm\mp(\text{LT}+\text{TL})}^{\text{Born}} &= \frac{128\pi\alpha^2}{s\beta^4} \frac{M_{\text{W}}^2}{s} \left\{ -\beta \cos \theta_{\text{cut}} + \frac{s^2 - 2M_{\text{W}}^2 s + 4M_{\text{W}}^4}{s^2} \log \left(\frac{1 + \beta \cos \theta_{\text{cut}}}{1 - \beta \cos \theta_{\text{cut}}} \right) \right. \\
&\quad \left. - \frac{4M_{\text{W}}^2 (s - 2M_{\text{W}}^2)}{s^2} \frac{\beta \cos \theta_{\text{cut}}}{1 - \beta^2 \cos^2 \theta_{\text{cut}}} \right\}, \tag{26}
\end{aligned}$$

and for the unpolarized cross-section

$$\sigma_{\text{unpol}}^{\text{Born}} = \frac{6\pi\alpha^2}{s} \left\{ \beta \cos \theta_{\text{cut}} - 4 \frac{M_{\text{W}}^2}{s} \left(1 - \frac{2M_{\text{W}}^2}{s} \right) \log \left(\frac{1 + \beta \cos \theta_{\text{cut}}}{1 - \beta \cos \theta_{\text{cut}}} \right) \right\}$$

²The second term in equation (6) of Ref. [7] should be multiplied by 2.

\sqrt{s}/GeV	θ	unpol	$\pm\pm\text{TT}$	$\pm\pm\text{LL}$	$\pm\mp\text{TT}$	$\pm\mp\text{LL}$	$\pm\mp(\text{LT} + \text{TL})$
500	$0^\circ < \theta < 180^\circ$	77.6	82.2	6.10×10^{-2}	70.2	9.99×10^{-1}	1.69
	$20^\circ < \theta < 160^\circ$	36.7	42.7	3.17×10^{-2}	28.2	9.89×10^{-1}	1.49
1000	$0^\circ < \theta < 180^\circ$	80.1	82.8	3.54×10^{-3}	76.9	2.52×10^{-1}	1.70×10^{-1}
	$20^\circ < \theta < 160^\circ$	14.2	16.8	7.18×10^{-4}	11.2	2.44×10^{-1}	1.21×10^{-1}
2000	$0^\circ < \theta < 180^\circ$	80.6	81.6	2.14×10^{-4}	79.5	6.41×10^{-2}	1.50×10^{-2}
	$20^\circ < \theta < 160^\circ$	4.07	4.84	1.27×10^{-5}	3.23	6.11×10^{-2}	8.26×10^{-3}

Table 1: Lowest-order integrated cross-sections in pb for several polarizations

$$+ \left\{ \left(\frac{1}{3} + \frac{M_W^4}{s^2} \right) \frac{16\beta \cos \theta_{\text{cut}}}{1 - \beta^2 \cos^2 \theta_{\text{cut}}} \right\}. \quad (27)$$

In Figs. 7 and 8 we show the lowest-order cross-sections for various polarizations and two different angular cuts $\theta_{\text{cut}} = 10^\circ, 20^\circ$. For $\theta_{\text{cut}} = 0$, the cross-sections for transverse W bosons approach a constant at high energies, $s \gg M_W^2$, owing to the massive t -channel exchange

$$\sigma_{\pm\pm\text{TT}}^{\text{Born}}, \sigma_{\pm\mp\text{TT}}^{\text{Born}} \xrightarrow{s \rightarrow \infty} \frac{8\pi\alpha^2}{M_W^2} = 80.8 \text{ pb}. \quad (28)$$

For a finite cut, $\sigma_{\pm\pm\text{TT}}^{\text{Born}}$ and $\sigma_{\pm\mp\text{TT}}^{\text{Born}}$ behave as $1/s$ for large s . The cross-sections $\sigma_{\pm\mp\text{LL}}^{\text{Born}}$ and $\sigma_{\pm\mp(\text{TL}+\text{LT})}^{\text{Born}}$ are proportional to $1/s$ and $1/s^2$, respectively, independently of the cut-off. The cross-section $\sigma_{\pm\pm\text{LL}}^{\text{Born}}$ goes like $1/s^2$ at high energies for $\theta_{\text{cut}} = 0$ and like $1/s^3$ for a finite cut-off. It is suppressed by about a factor of 10^3 at $E_{\text{CMS}} = 500$ GeV. Note that the latter cross-section can be enhanced drastically by non-standard physics [12]. At high energies, the unpolarized cross-section $\sigma_{\text{unpol}}^{\text{Born}}$ is dominated by transverse W bosons, and all polarized cross-sections involving two transverse W bosons are of the same order-of-magnitude. Close to threshold the differential and integrated cross-sections for all polarization configurations vanish like β . Numerical values for the lowest-order cross-sections can be found in Table 1.

Figures 9 and 10 show the angular distributions of the differential lowest-order cross-sections for various polarizations at $E_{\text{CMS}} = 500, 1000$ and 2000 GeV. The cross-sections involving transverse W bosons are characterized by the t - and u -channel poles in the forward and backward directions, respectively. With increasing energy they increase in the very forward and backward direction proportional to s but decrease in the central angular region proportional to $1/s$. The respective behavior of $(d\sigma/d\Omega)_{\pm\pm\text{LL}}^{\text{Born}}$ is $1/s$ and $1/s^3$. The cross-sections $(d\sigma/d\Omega)_{\pm\mp\text{LL}}^{\text{Born}}$ and $(d\sigma/d\Omega)_{\pm\mp(\text{LT}+\text{TL})}^{\text{Born}}$ vanish in the forward and backward direction. While $(d\sigma/d\Omega)_{\pm\mp\text{LL}}^{\text{Born}}$ reach their maxima at 90° and decrease proportional to $1/s$ for all angles, $(d\sigma/d\Omega)_{\pm\mp(\text{LT}+\text{TL})}^{\text{Born}}$ possess maxima at $|\cos \theta| = \beta$ decreasing proportional to $1/s$ and relative minima at $\theta = 90^\circ$ decreasing proportional to $1/s^2$.

4 Radiative corrections

4.1 Non-linear gauge fixing

We have performed the calculation of the radiative corrections in tHF gauge and a NL gauge with the gauge-fixing term given in equation (20) applying the complete on-shell renormalization scheme in both cases [17]. As pointed out in Sect. 2 the $\phi^\pm W^\mp A$ vertices vanish in NL gauge. As a consequence the ϕ self-energy and the ϕW mixing energy do not contribute, and the number of vertex and box diagrams is reduced from 441 in tHF gauge to 268 in NL gauge (for one fermion generation).

Furthermore, the analytical expressions for the $W^\pm \bar{u}^\pm u^{A,Z}$ vertices (with \bar{u}, u denoting the Fadeev–Popov ghost fields) are proportional to the W-boson momentum in NL gauge and thus vanish for on-shell W bosons. For this reason most of the box and vertex diagrams with internal ghost fields vanish. As the corrections to the AAA and AAZ vertices vanish in both gauges, the number of non-vanishing vertex and box diagrams reduces to 365 in tHF gauge and to 168 in NL gauge. Moreover, many diagrams have a simpler structure in NL gauge.

In order to determine the counterterms necessary for renormalization one has to calculate the self-energies. Here we list the differences $\Delta\Sigma = \Sigma^{\text{NL}} - \Sigma^{\text{tHF}}$ between the self-energies in NL gauge and the ones in tHF gauge. The transverse parts of the latter can be found e.g. in Ref. [17]. For the transverse part of the W self-energy we find

$$\Delta\Sigma_{\text{T}}^{WW} = \frac{\alpha}{2\pi}(k^2 - M_{\text{W}}^2) \left[B_0(k^2, 0, M_{\text{W}}) + \frac{c_{\text{W}}^2}{s_{\text{W}}^2} B_0(k^2, M_{\text{Z}}, M_{\text{W}}) \right], \quad (29)$$

and for its longitudinal part

$$\begin{aligned} \Delta\Sigma_{\text{L}}^{WW} = & -\frac{\alpha}{4\pi} \left\{ \frac{c_{\text{W}}^2}{s_{\text{W}}^2} (5k^2 + 5M_{\text{Z}}^2 - 3M_{\text{W}}^2) B_0(k^2, M_{\text{W}}, M_{\text{Z}}) + (5k^2 - 3M_{\text{W}}^2) B_0(k^2, M_{\text{W}}, 0) \right. \\ & \left. + \frac{5}{s_{\text{W}}^2} M_{\text{W}}^2 [B_0(0, 0, M_{\text{W}}) - B_0(0, 0, M_{\text{Z}})] - \frac{2}{s_{\text{W}}^2} k^2 \right\}, \end{aligned} \quad (30)$$

where B_0 is the scalar one-loop two-point function [17, 18]. The differences for the self-energies involving neutral gauge bosons can be given in a compact way

$$\Delta\Sigma_{\text{T}}^{BB'} = -\frac{\alpha}{2\pi} f^{BB'} (2k^2 - M_{\text{B}}^2 - M_{\text{B}'}^2) B_0(k^2, M_{\text{W}}, M_{\text{W}}), \quad (31)$$

$$\Delta\Sigma_{\text{L}}^{BB'} = \frac{\alpha}{2\pi} f^{BB'} (M_{\text{B}}^2 + M_{\text{B}'}^2) B_0(k^2, M_{\text{W}}, M_{\text{W}}), \quad (32)$$

with $B^{(\prime)} = A, Z$ and

$$f^{AA} = 1, \quad f^{AZ} = -\frac{c_{\text{W}}}{s_{\text{W}}}, \quad f^{ZZ} = \frac{c_{\text{W}}^2}{s_{\text{W}}^2}. \quad (33)$$

Note that the differences for the transverse parts of the W, Z, and A self-energies are proportional to $(k^2 - M_{\text{W,Z}}^2)$ and k^2 , respectively.

4.2 Inventory of $\mathcal{O}(\alpha)$ corrections

In the following we list the virtual corrections, i.e. the contributions to $\delta\mathcal{M}$, in NL gauge. We adopt the conventions of Ref. [17], where the necessary explicit results for

the transverse parts of the self-energies and the renormalization constants can be found. Because of the length of our results we do not explicitly write down the analytic expressions.

Owing to our renormalization scheme, we have to deal with self-energy insertions only into the internal lines of the tree diagrams of Fig. 1. These result in the following contribution to the invariant matrix element

$$\delta\mathcal{M}_{\text{self}} = 4\pi\alpha \left\{ \frac{2s}{(M_W^2 - t)^2} \Sigma_T^{WW}(t) \mathcal{M}_{0,t} + \frac{2s}{(M_W^2 - u)^2} \Sigma_T^{WW}(u) \mathcal{M}_{0,u} \right. \\ \left. + \frac{1}{t} (\Sigma_T^{WW}(t) - \Sigma_L^{WW}(t)) \mathcal{M}_{0000}^{(t)} + \frac{1}{u} (\Sigma_T^{WW}(u) - \Sigma_L^{WW}(u)) \mathcal{M}_{0000}^{(u)} \right\}. \quad (34)$$

Figure 2 shows the t -channel graphs for the upper AWW^* vertex (asterics denote off-shell fields); the diagrams (h), (i), (k), (l), and (n) vanish for on-shell external photons and W bosons. The diagrams for the lower AWW^* vertex can be constructed in an analogous way, and the u -channel diagrams are obtained via crossing, i.e. the interchange of the two external photons.

The AAA^* and AAZ^* vertex corrections vanish according to Yang's theorem [19] and because the virtual A and Z are coupled to a conserved current. Thus, the only s -channel vertex corrections, which contribute to $\delta\mathcal{M}$, are the Higgs-resonant AAH^* -vertex graphs shown in Fig. 5. For the graphs (a)–(d) also crossed ones exist. The AAH^* corrections are discussed in the next subsection.

The box diagrams are shown in Figs. 3 and 4. While to each diagram in Fig. 3 a crossed partner diagram corresponds, those in Fig. 4 are symmetric under crossing. For on-shell external bosons the graphs (h) and (i) of Fig. 3 and the graphs (e) and (f) of Fig. 4 vanish.

The renormalization is performed in the on-shell renormalization scheme. Evaluation of the counterterms diagrams yields

$$\delta\mathcal{M}_{\text{counter}} = \mathcal{M}_{\text{Born}} \left(2\delta Z_e + \delta Z_W + \delta Z_{AA} - \frac{c_W}{s_W} \delta Z_{ZA} \right) \\ - 8\pi\alpha \left(\frac{s\delta M_W^2}{(M_W^2 - t)^2} \mathcal{M}_{0,t} + \frac{s\delta M_W^2}{(M_W^2 - u)^2} \mathcal{M}_{0,u} \right). \quad (35)$$

In this context we mention that the massive gauge-boson sector does not break electromagnetic gauge invariance if the NL gauge fixing (20) is applied. As a consequence on-shell photons do not mix with Z bosons rendering the counterterm δZ_{ZA} zero,

$$\delta Z_{ZA} = 2 \frac{\Sigma_T^{AZ}(0)}{M_Z^2} = 0. \quad (36)$$

The charge renormalization constant δZ_e is then given by [17]

$$\delta Z_e = -\frac{1}{2} \delta Z_{AA} = \frac{1}{2} \frac{\partial \Sigma_T^{AA}(k^2)}{\partial k^2} \Big|_{k^2=0}, \quad (37)$$

so that the complete counterterm contribution to the matrix element \mathcal{M} reduces to

$$\delta\mathcal{M}_{\text{counter}}^{\text{NL}} = \mathcal{M}_{\text{Born}} \delta Z_W - 8\pi\alpha \left(\frac{s\delta M_W^2}{(M_W^2 - t)^2} \mathcal{M}_{0,t} + \frac{s\delta M_W^2}{(M_W^2 - u)^2} \mathcal{M}_{0,u} \right). \quad (38)$$

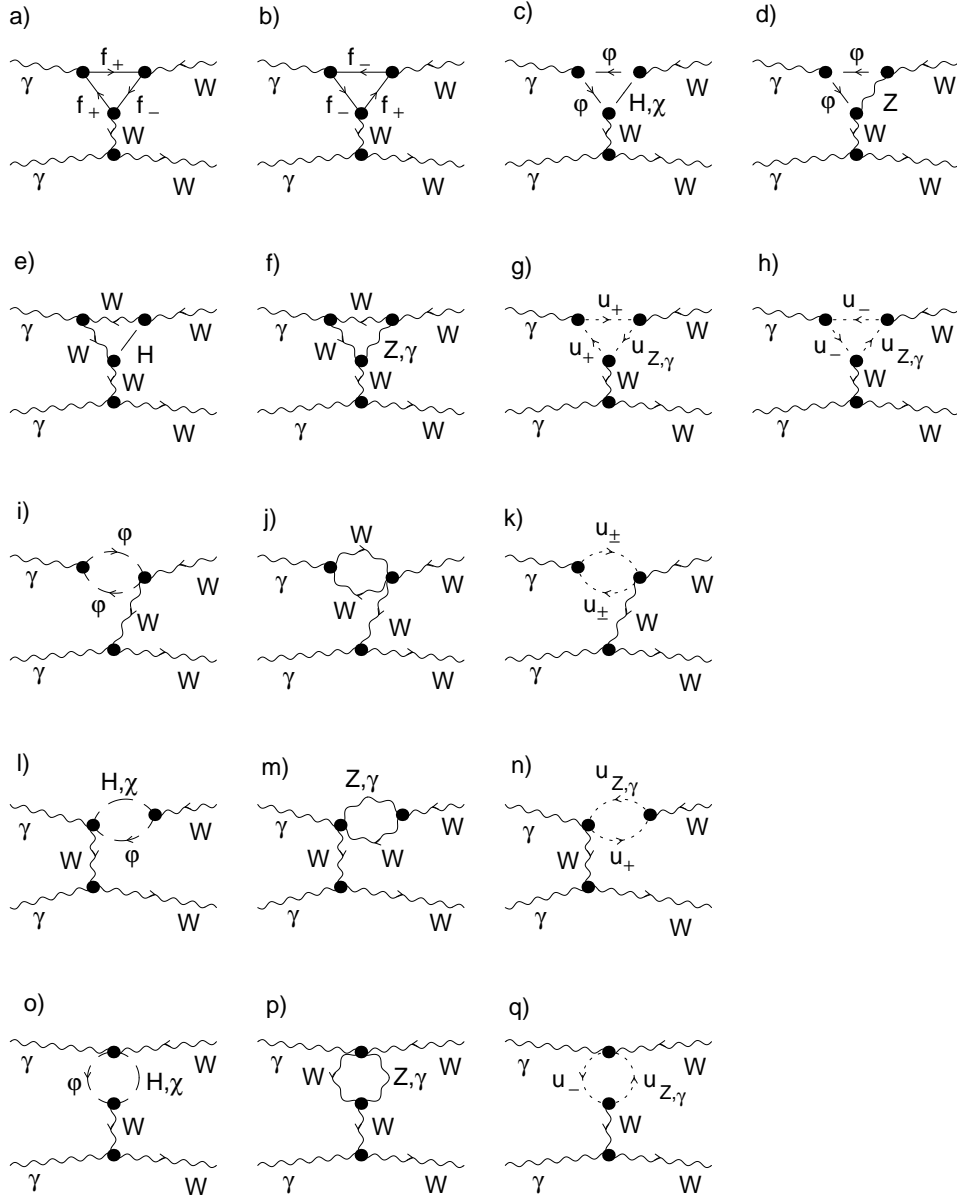


Figure 2: The t -channel diagrams for the upper AWW^* vertex

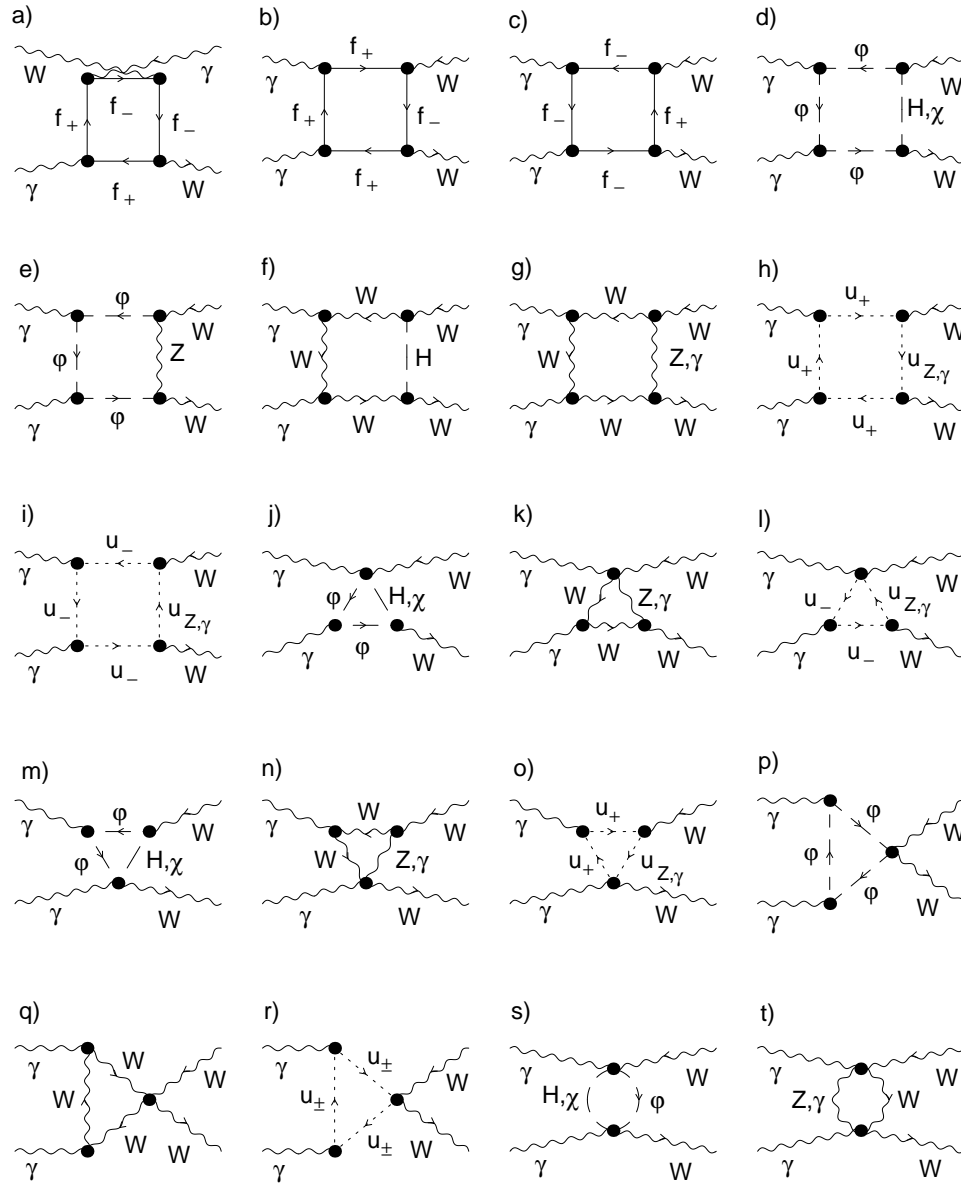


Figure 3: Non-crossing-symmetric box diagrams

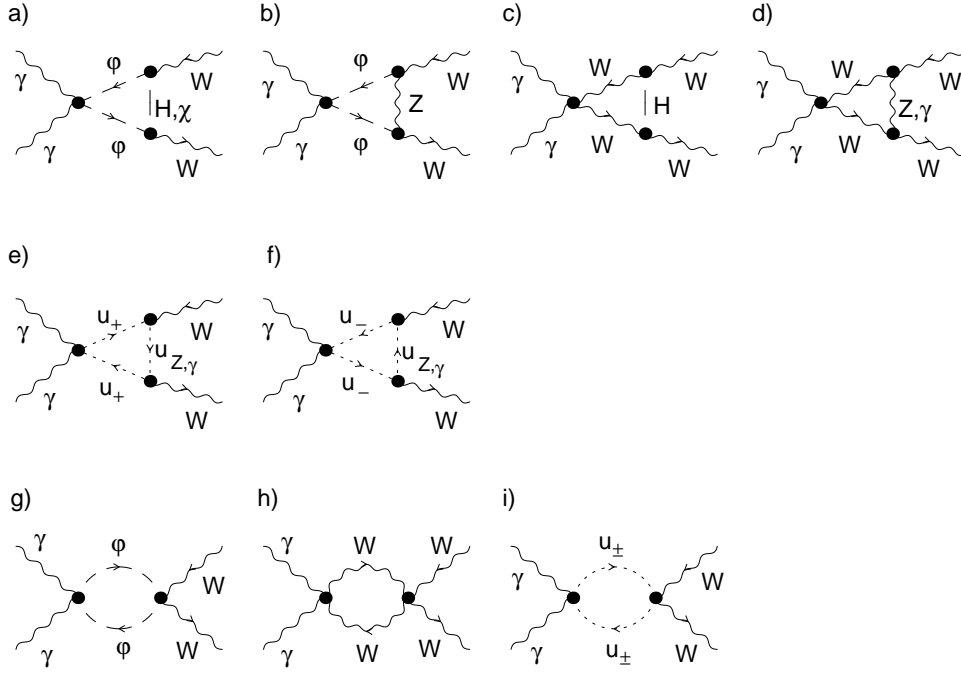


Figure 4: Crossing-symmetric box diagrams

4.3 Higgs resonance

The Higgs resonance in $\gamma\gamma \rightarrow W^+W^-$ was discussed extensively in the literature; see e.g. Refs. [10, 11]. So we restrict ourselves to the listing of our results for the Higgs-resonant graphs.

The Higgs-resonant part of the process is caused by the graphs of Fig. 5. These yield a contribution of the form (compare Ref. [11])

$$\delta\mathcal{M}_{AAH^*} = \frac{F^H(s)}{s - M_H^2} \mathcal{M}_{0000} \quad (39)$$

with

$$F^H(s) = -\frac{\alpha^2}{s_W^2} \left\{ 6M_W^2 + M_H^2 + M_W^2 C^{(\text{gauge})} C_0(s, 0, 0, M_W^2, M_W^2, M_W^2) \right. \\ \left. - 2 \sum_f N_f^c Q_f^2 m_f^2 \left[2 + (4m_f^2 - s) C_0(s, 0, 0, m_f^2, m_f^2, m_f^2) \right] \right\}. \quad (40)$$

The sum in (40) extends over all massive fermions with charge Q_f and color factor N_f^c . The coefficient $C^{(\text{gauge})}$ is gauge-dependent and reads

$$C^{(\text{gauge})} = 12M_W^2 + 2M_H^2 - 8s \quad (41)$$

in NL gauge and

$$C^{(\text{gauge})} = 12M_W^2 + M_H^2 - 7s \quad (42)$$

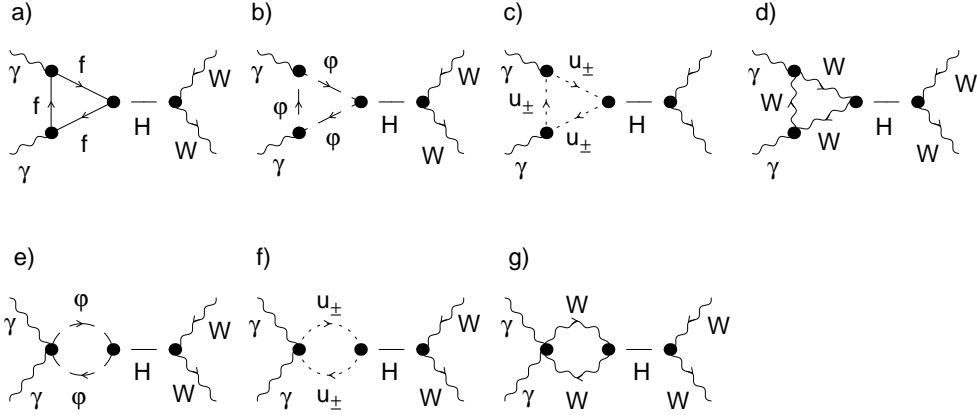


Figure 5: The AAH^* vertex diagrams

in tHF gauge. Note that $\delta\mathcal{M}_{AAH^*}$ vanishes for opposite helicities of the incoming photons or outgoing W bosons together with \mathcal{M}_{0000} . Hence the Higgs resonance is only present for photons and W bosons with equal helicities.

In the literature [9, 10, 11], the Higgs-boson width has been introduced naïvely by the replacement

$$\frac{F^H(s)}{s - M_H^2} \rightarrow \frac{F^H(s)}{s - M_H^2 + iM_H\Gamma_H} \quad (43)$$

in (39). Owing to the gauge dependence of $F^H(s)$, this treatment destroys gauge invariance. The violation of gauge invariance occurs at the level of the non-resonant $\mathcal{O}(\alpha)$ corrections, which were neglected in Refs. [9, 10, 11]. Since our main concern are exactly these corrections we have to take care of gauge invariance. To this end we decompose (39) into a gauge-invariant resonant part and a gauge-dependent non-invariant part and introduce Γ_H only in the former. This results in the following replacement in (39)

$$\frac{F^H(s)}{s - M_H^2} \rightarrow \frac{F^H(M_H^2)}{s - M_H^2 + iM_H\Gamma_H} + \frac{F^H(s) - F^H(M_H^2)}{s - M_H^2}. \quad (44)$$

Equations (39) and (44) yield a gauge-invariant amplitude including the finite width in the resonant Higgs contributions.

Since the resonant Higgs contributions are large for $s \approx M_H^2$, we take also the square of the resonant part of the matrix element into account in the numerical analysis [compare (47)].

For a calculation with order $\mathcal{O}(\alpha)$ accuracy also near $s = M_H^2$, one should take into account the $\mathcal{O}(\alpha)$ corrections to the Higgs-boson width [20] and to $F^H(M_H^2)$ in the resonant contribution. Since the Higgs resonance is not our main concern, we only take into account the lowest-order decay width determined from the imaginary part of the one-loop Higgs-boson self-energy and (40) for $F^H(M_H^2)$.

4.4 Leading corrections

The electroweak radiative corrections typically involve leading contributions of universal origin such as the leading-logarithmic QED corrections, corrections arising from the running of α , corrections associated with large top-quark or Higgs-boson masses, and the Coulomb singularity at threshold for the production of a pair of charged particles.

We first discuss the leading weak corrections:

- For $\gamma\gamma \rightarrow W^+W^-$, the running of α is not relevant, as the *two* external photons are on mass shell, i.e. the relevant effective coupling is the one at zero-momentum transfer. Technically, the large logarithms present in the renormalization constant δZ_e of the electron charge are canceled by the corresponding logarithms in the wave-function renormalization constant δZ_{AA} of the external photons, as can be explicitly seen in (37).
- The Higgs-mass-dependent corrections have been discussed in detail in Ref. [12]. In the heavy-Higgs limit, $M_H \gg \sqrt{s}$, no corrections involving $\log(M_H/M_W)$ or M_H^2/M_W^2 arise. Consequently the Higgs-mass dependence is small. However, for $\sqrt{s} \gg M_H \gg M_W$ corrections proportional to M_H^2/M_W^2 appear for the cross-sections involving longitudinal gauge bosons as a remnant of the unitarity cancellations (compare Ref. [21]). These give rise to large effects in particular for $\sigma_{\pm\pm LL}$.
- The situation is similar for the top-dependent corrections. As the lowest-order matrix element is independent of the weak mixing angle, no universal corrections proportional to m_t^2/M_W^2 arise from renormalization. It can be easily derived by power counting that such terms do also not result from loop diagrams in the heavy top limit $m_t \gg \sqrt{s}$. A more accurate analysis reveals that even no terms involving $\log(m_t/M_W)$ occur in this limit. On the other hand, for $\sqrt{s} \gg m_t \gg M_W$ corrections proportional to m_t^2/M_W^2 appear for longitudinal gauge bosons (compare Ref. [21]).

All these statements hold in the on-shell renormalization scheme with α , M_W and M_Z as input parameters. If the M_W mass is determined from G_μ , corrections involving logarithms of the light fermion masses, m_t , and M_H occur together with the universal corrections proportional to m_t^2/M_W^2 associated with the ρ parameter.

The leading corrections of electromagnetic origin are independent of the renormalization scheme and the input parameters:

- As $\gamma\gamma \rightarrow W^+W^-$ involves no light charged external particles, no large logarithmic corrections associated with collinear photons show up apart from the region of very high energies, $s \gg M_W^2$. As a consequence, the photonic corrections are not enhanced with respect to the weak corrections.
- Close to threshold, the Coulomb singularity gives rise to large effects as in any pair-production process of charged particles. These effects can be extracted on general grounds or directly from the Feynman diagrams. To this end one has to consider all diagrams resulting from the lowest-order diagrams with an additional photon exchanged between the final state W bosons (Fig. 6). In the limit $\beta \ll 1$ one obtains:

$$\delta\sigma^{\text{Coul.}} = \frac{\alpha\pi}{2\beta}\sigma^{\text{Born}}. \quad (45)$$

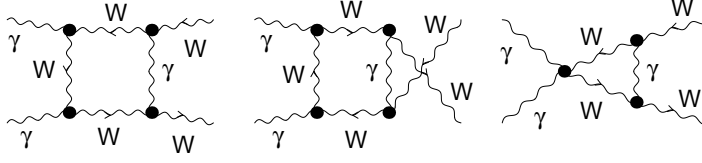


Figure 6: The diagrams that contribute to the Coulomb singularity in NL gauge

The β^{-1} correction factor in (45) to the Born cross-section near threshold is typical for the pair production of stable (on-shell) particles. The generalization to unstable (off-shell) particles can be found in the literature [22].

At high energies, $s \gg M_W^2$, the radiative corrections are dominated by terms like $(\alpha/\pi) \log^2(s/M_W^2)$, which arise from vertex and box diagrams (comp. Ref. [21]). At 1 TeV these are about 10%, setting the scale for the (weak) radiative corrections at this energy.

4.5 Structure of the final result

For a consistent treatment of the virtual one-loop radiative corrections the squared transition matrix element has to be expanded in a power series of the coupling constant α

$$|\mathcal{M}|^2 = |\mathcal{M}_{\text{Born}}|^2 + 2 \text{Re}\{\delta\mathcal{M}\mathcal{M}_{\text{Born}}^*\} + \text{higher orders.} \quad (46)$$

The $\mathcal{O}(\alpha)$ correction $\delta\mathcal{M}$ to the matrix element \mathcal{M} is decomposed as in (4). We do not consider those polarization configurations for which the lowest-order matrix element vanishes.

The invariant functions F_{ijkl} are calculated in terms of standard tensor integrals, which are reduced to scalar integrals by the procedure proposed in Ref. [23]. The scalar one-loop integrals are evaluated using the methods and general results of Ref. [18]. Whereas UV divergences are regularized dimensionally, we treat IR divergences by introducing an infinitesimal photon mass λ . The artificial λ dependence drops out when soft-photon bremsstrahlung is added.

The cross-section including full $\mathcal{O}(\alpha)$ corrections and the squared Higgs-resonant $\mathcal{O}(\alpha)$ contributions read

$$\begin{aligned} \left(\frac{d\sigma}{d\Omega}\right) &= \frac{\beta}{64\pi^2 s} \sum_{\lambda_1\lambda_2\lambda_3\lambda_4} \left[|\mathcal{M}_{\text{Born}}|^2 (1 + \delta_{\text{SB}}) + 2 \text{Re}\{\delta\mathcal{M}\mathcal{M}_{\text{Born}}^*\} + \frac{|F^H(M_H^2)\mathcal{M}_{0000}|^2}{(s - M_H^2)^2 + \Gamma_H^2 M_H^2} \right] \\ &= \left(\frac{d\sigma}{d\Omega}\right)^{\text{Born}} (1 + \delta), \end{aligned} \quad (47)$$

where

$$\begin{aligned} \delta_{\text{SB}} &= -\frac{\alpha}{\pi} \left\{ 2 \log \frac{2\Delta E}{\lambda} + \frac{1}{\beta} \log \left(\frac{1-\beta}{1+\beta} \right) + \frac{s - 2M_W^2}{s\beta} \left[2 \log \frac{2\Delta E}{\lambda} \log \left(\frac{1-\beta}{1+\beta} \right) \right. \right. \\ &\quad \left. \left. - 2\text{Li}_2 \left(\frac{1-\beta}{1+\beta} \right) + \frac{1}{2} \log^2 \left(\frac{1-\beta}{1+\beta} \right) + \frac{\pi^2}{3} - 2 \log \left(\frac{1-\beta}{1+\beta} \right) \log \left(\frac{2\beta}{1+\beta} \right) \right] \right\} \end{aligned} \quad (48)$$

denotes the soft-photon correction factor, ΔE is the maximal energy of the emitted photon, F^H is given in (40), and δ is the relative correction.

For the integrated cross-section σ , the relative correction is defined analogously

$$\sigma = \int_{\theta_{\min}}^{\theta_{\max}} d\cos\theta \int_0^{2\pi} d\phi \left(\frac{d\sigma}{d\Omega} \right) = \sigma^{\text{Born}}(1 + \delta). \quad (49)$$

In order to ensure the correctness of our results we have performed three different calculations. The corrections were calculated with *FeynCalc* [15] both in tHF gauge and NL gauge (20). A further calculation was performed independently with *Mathematica* without using *FeynCalc* in NL gauge. The results of these various calculations agree numerically within 8–9 digits for the corrected cross-section. Moreover, we have checked that all UV and IR singularities cancel, and that the symmetries discussed in Section 2 hold. Finally, the leading corrections discussed in Section 4.4 have been deduced analytically and checked numerically.

5 Numerical results

For the numerical evaluation we used the following set of parameters [24]

$$\begin{aligned} \alpha &= 1/137.0359895 & G_\mu &= 1.166390 \times 10^{-5} \text{ GeV}^{-2} \\ M_Z &= 91.187 \text{ GeV}, & M_H &= 250 \text{ GeV}, \\ m_e &= 0.51099906 \text{ MeV}, & m_\mu &= 105.65839 \text{ MeV}, & m_\tau &= 1.777 \text{ GeV}, \\ m_u &= 46.0 \text{ MeV}, & m_c &= 1.50 \text{ GeV}, & m_t &= 170 \text{ GeV}, \\ m_d &= 46.0 \text{ MeV}, & m_s &= 150 \text{ MeV}, & m_b &= 4.50 \text{ GeV}. \end{aligned} \quad (50)$$

The masses of the light quarks are adjusted such that the experimentally measured hadronic vacuum polarization is reproduced [25]. As discussed in the previous section, no large logarithms associated with fermion masses enter the $\mathcal{O}(\alpha)$ corrections for $\gamma\gamma \rightarrow W^+W^-$ in the on-shell renormalization scheme, and the fermion mass contributions are only of the order $\alpha m_f^2/M_W^2$. However, as the Fermi-constant G_μ is empirically much better known than the W mass, M_W is usually calculated from all the other parameters using the muon decay width including radiative corrections. In this calculation of M_W all parameters given above enter sensibly. If not stated otherwise, M_W is determined in the following using formulae (2.56) and (2.57) of Ref. [26]. The above set of parameters yields

$$M_W = 80.333 \text{ GeV}.$$

As discussed above, no leading collinear logarithms occur in $\gamma\gamma \rightarrow W^+W^-$. Thus, the only source of enhanced photonic corrections are the soft-photon-cut-off-dependent terms which yield the following relative correction

$$\delta_{\text{cut}} = -\frac{2\alpha}{\pi} \log \frac{\Delta E}{E} \left(1 - \frac{s - 2M_W^2}{s\beta} \log \frac{1 + \beta}{1 - \beta} \right). \quad (51)$$

While these cut-off-dependent terms are definitely of electromagnetic origin, the complete electroweak $\mathcal{O}(\alpha)$ corrections cannot be separated on the basis of Feynman diagrams in

a gauge-invariant way. Since we are mainly interested in the weak corrections we discard the cut-off-dependent terms (51) and consider the rest as a suitable measure of the weak corrections for the process at hand. The elimination of the cut-off-dependent terms can be achieved simply by setting the soft-photon cut-off energy equal to the beam energy. If not stated otherwise, the correction δ stands in the following for the complete soft-photonic and virtual electroweak corrections as defined in (47) for $\Delta E = E$.

Figure 7 shows the corrections to the total cross-sections integrated over $10^\circ \leq \theta \leq 170^\circ$ for different boson polarizations. The dominating channels involving transverse W bosons get corrections which almost coincide with each other as well as the unpolarized case and reach roughly -20% at $\sqrt{s} = 2 \text{ TeV}$. For $\theta_{\text{cut}} = 10^\circ$ the corrections to $\sigma_{\pm\mp\text{LL}}$ are similar, and those to $\sigma_{\pm\mp(\text{LT}+\text{TL})}$ are only slightly larger. The corrections to $\sigma_{\pm\pm\text{LL}}$ are completely different. At low energies they are dominated by the Higgs resonance, at high energies by corrections proportional to $M_{\text{H}}^2/M_{\text{W}}^2$ which are additionally enhanced owing to the suppression of the corresponding lowest-order cross-section. This cross-section, which is also most sensitive to a very heavy Higgs boson, has been discussed in detail in Ref. [12]. Note that owing to helicity conservation only the cross-sections with equal photon and W boson helicities are affected by the Higgs resonance.

Imposing a more stringent angular cut $20^\circ < \theta < 160^\circ$ to the phase-space integration, the corrections become larger at high energies for all polarizations involving t - and u -channel poles and reach about -35% at $\sqrt{s} = 2 \text{ TeV}$ (Fig. 8). This is due to the fact that after cutting off the dominant forward and backward peaks we are left with a region in phase space where the influence of the radiative corrections becomes more important. The corrections to the other cross-sections, in particular to $\sigma_{\pm\mp\text{LL}}$, are hardly affected.

In Figs. 9 and 10 we show the corrections to the differential cross-sections for $\sqrt{s} = 0.5, 1$ and 2 TeV . Whenever the differential cross-section is sizable, δ is of the order of 10% . The corrections are in particular small in the forward and backward direction for all cross-sections that involve t - and u -channel poles in lowest order. On the other hand, the corrections get very large when the lowest-order cross-section is suppressed or tends to zero, in particular for $d\sigma_{\pm\pm\text{LL}}/d\Omega$ at high energies and intermediate scattering angles. The maximal corrections are usually reached for central values of the scattering angle. In accordance with the discussion in Section 2, the corrections are forward-backward symmetric for equal photon helicities. For opposite photon helicities they include an asymmetric contribution originating from box diagrams and AWW vertex corrections involving fermion loops. The corrections for two negative helicity photons are equal to those for two positive helicity photons. As a consequence of Bose symmetry, the corrections to $d\sigma_{+-}/d\Omega$ are obtained from those to $d\sigma_{-+}/d\Omega$ upon exchanging u and t , i.e. $\theta \leftrightarrow 180^\circ - \theta$. Thus, the unpolarized cross-section is forward-backward-symmetric.

In Table 2 we list the unpolarized cross-section and the corresponding corrections for several energies and scattering angles. We include the corrections for a soft-photon-energy cut-off $\Delta E = 0.1E$, the cut-off-dependent corrections δ_{cut} from (51), and the individual (gauge-invariant) fermionic δ_{ferm} and bosonic corrections δ_{bos} . The fermionic corrections consist of all loop diagrams and counterterm contributions involving fermion loops, all other contributions form the bosonic corrections. The fermionic corrections stay below 5–10% even for high energies. On the other hand, the bosonic contributions are responsible for the large corrections at high energies, in particular in the central angular region.

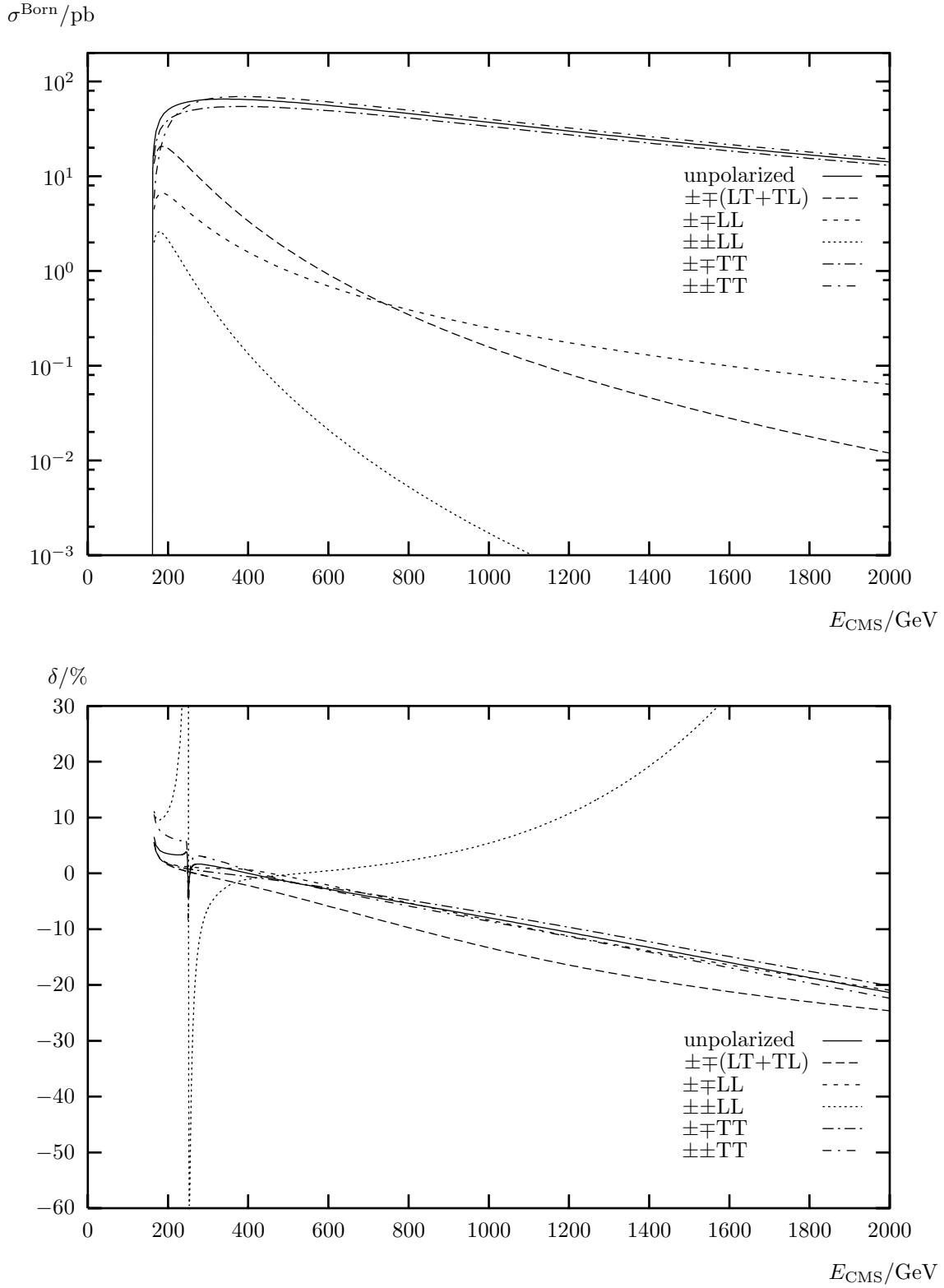


Figure 7: Integrated lowest-order cross-sections and corresponding relative corrections for several polarizations with an angular cut $10^\circ \leq \theta \leq 170^\circ$

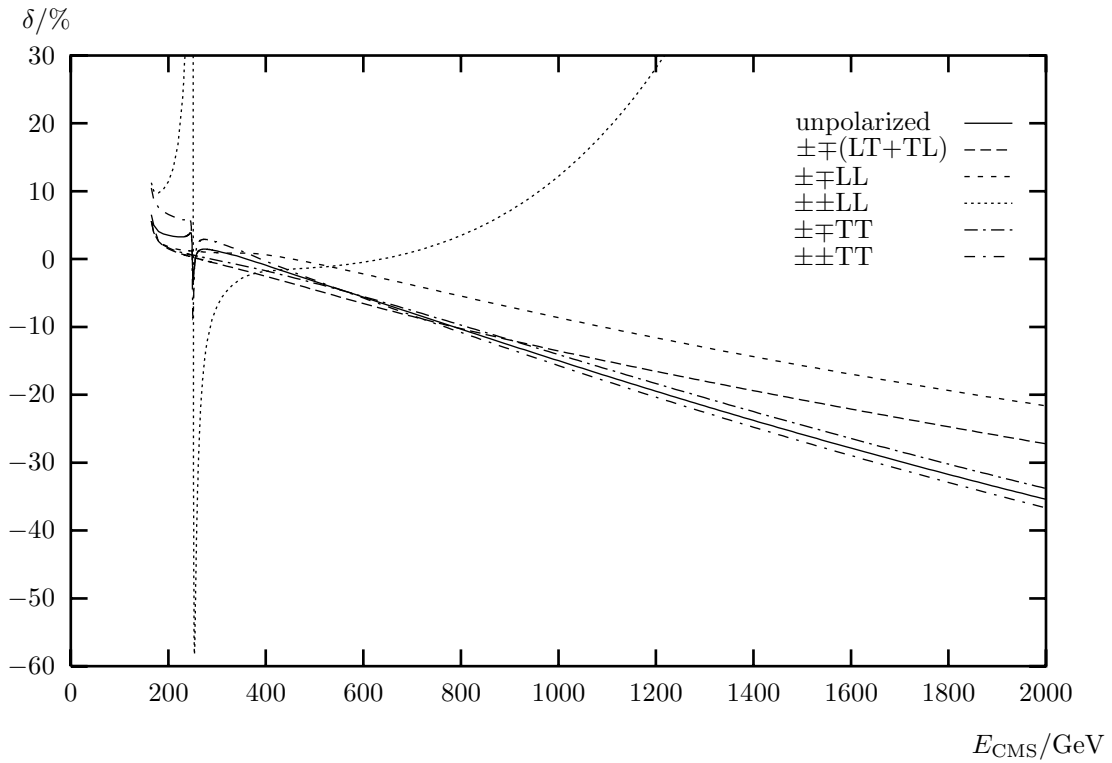
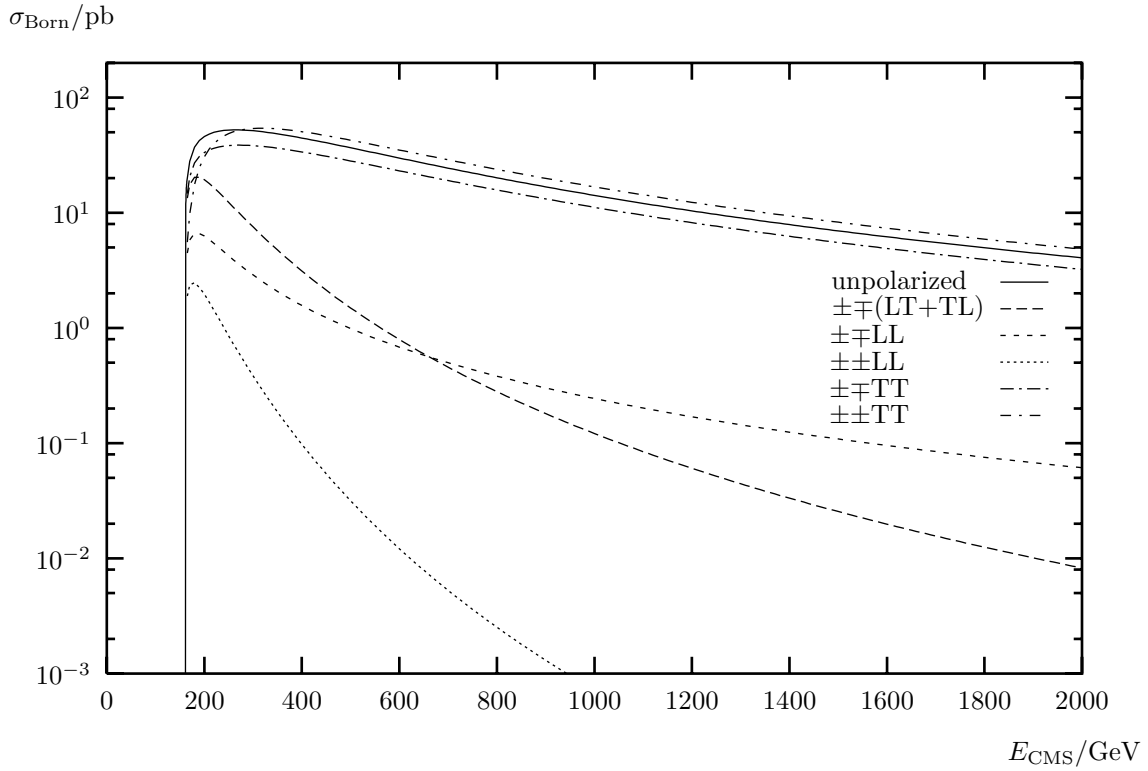


Figure 8: Same as in Fig. 7 but with an angular cut $20^\circ \leq \theta \leq 160^\circ$

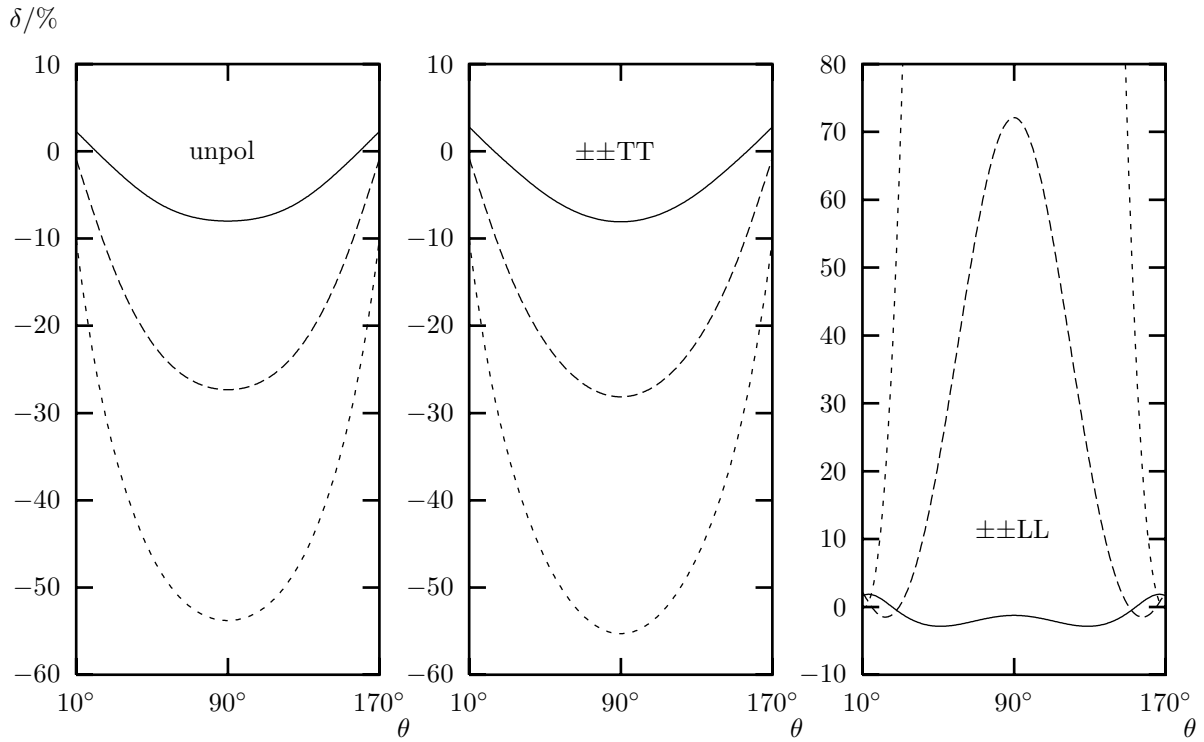
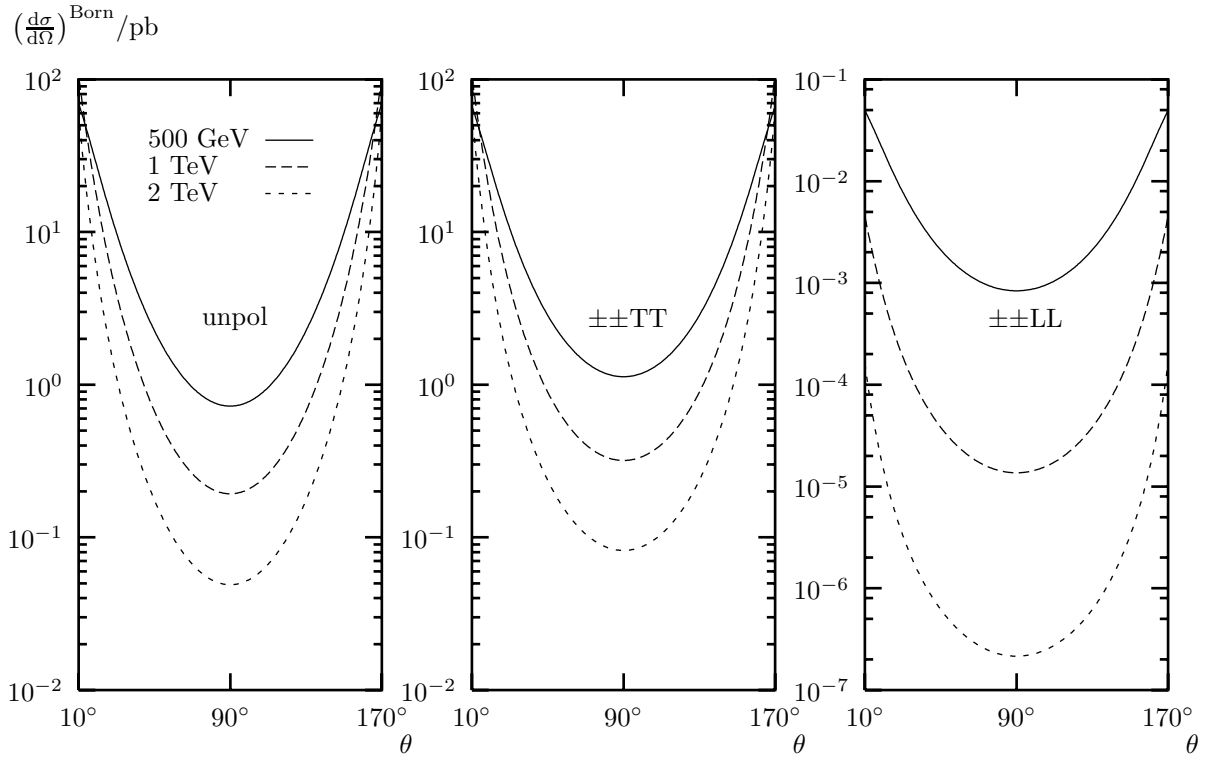


Figure 9: Differential lowest-order cross-sections and relative corrections for the unpolarized cross-section and the cross-sections with equal photon helicities

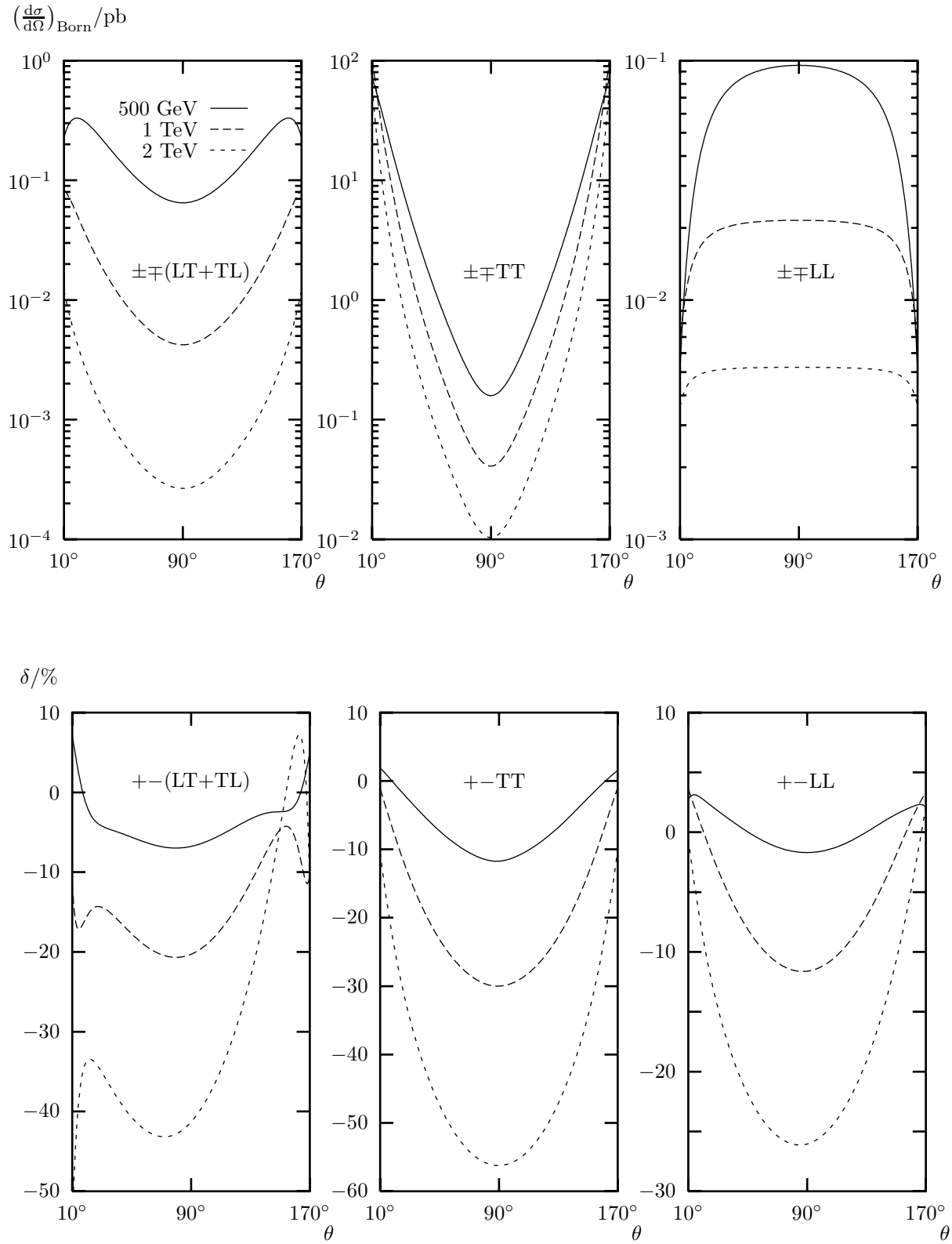


Figure 10: Differential lowest-order cross-sections and relative corrections for the cross-sections with opposite photon helicities

\sqrt{s}/GeV	θ	$\sigma^{\text{Born}}/\text{pb}$	$\delta_{\Delta E=0.1E}/\%$	$\delta_{\text{cut}}/\%$	$\delta_{\Delta E=E}/\%$	$\delta_{\text{bos}}/\%$	$\delta_{\text{ferm}}/\%$
500	5°	98.13	0.02	-2.79	2.81	1.49	1.32
	20°	26.04	-2.68	-2.79	0.11	-0.08	0.19
	90°	0.724	-10.79	-2.79	-8.00	-5.62	-2.38
	$0^\circ < \theta < 180^\circ$	77.55	-3.38	-2.79	-0.59	-0.65	0.06
	$10^\circ < \theta < 170^\circ$	60.74	-4.27	-2.79	-1.48	-1.21	-0.27
	$20^\circ < \theta < 160^\circ$	36.67	-6.06	-2.79	-3.27	-2.39	-0.89
1000	5°	291.9	-2.06	-4.31	2.25	1.04	1.21
	20°	15.61	-11.90	-4.31	-7.59	-6.37	-1.22
	90°	0.193	-31.64	-4.31	-27.33	-21.93	-5.40
	$0^\circ < \theta < 180^\circ$	80.05	-7.08	-4.31	-2.77	-2.71	-0.06
	$10^\circ < \theta < 170^\circ$	37.06	-12.26	-4.31	-7.95	-6.65	-1.30
	$20^\circ < \theta < 160^\circ$	14.16	-19.29	-4.31	-14.98	-12.20	-2.78
2000	5°	418.8	-7.14	-5.80	-1.33	-1.59	0.25
	20°	5.163	-30.31	-5.80	-24.51	-20.96	-3.55
	90°	0.049	-59.59	-5.80	-53.78	-45.47	-8.32
	$0^\circ < \theta < 180^\circ$	80.59	-9.85	-5.80	-4.04	-3.95	-0.09
	$10^\circ < \theta < 170^\circ$	14.14	-27.15	-5.80	-21.35	-18.34	-3.01
	$20^\circ < \theta < 160^\circ$	4.068	-41.22	-5.80	-35.41	-30.12	-5.29

Table 2: Lowest-order cross-sections and relative corrections for unpolarized particles

In Ref. [6] various observables have been investigated in view of their sensitivity to anomalous couplings, involving the total cross-section and the following ratios³

$$R_{\text{IO}} = \frac{\sigma(|\cos \theta| < 0.4)}{\sigma(|\cos \theta| < 0.8)}, \quad (52)$$

$$R_{\text{LT}} = \frac{\sigma_{\text{LL}}}{\sigma_{\text{TT}}}, \quad (53)$$

$$R_{02} = \frac{\sigma_{++}}{\sigma_{+-}}. \quad (54)$$

We list the lowest-order predictions together with the $\mathcal{O}(\alpha)$ -corrected ones and the relative corrections for these observables in Table 3 using $|\cos \theta_{\text{cut}}| = 0.8$.

In Tables 4 – 7 we show the variation of the SM corrections with the top-quark and Higgs-boson masses at $\sqrt{s} = 500$ GeV in per cent of the cross-section for our standard set of parameters (50). We have determined this variation by searching the maximum and minimum cross-sections in the range $130 \text{ GeV} < m_t < 210 \text{ GeV}$ for the variation with m_t and in the ranges $60 \text{ GeV} < M_H < 400 \text{ GeV}$ and $600 \text{ GeV} < M_H < 1000 \text{ GeV}$ for the variation with M_H . The range $400 \text{ GeV} < M_H < 600 \text{ GeV}$ has been left out as there the Higgs-mass dependence is dominated by the Higgs resonance. Because the resonance

³Note that we do not perform a convolution with a realistic photon spectrum but consider the incoming photons as monochromatic.

\sqrt{s}/GeV		σ/pb	R_{IO}	R_{LT}	R_{02}
500	Born level	15.74	0.265	0.0308	1.934
	corrected	14.82	0.259	0.0325	1.950
	corrections/%	-5.83	-2.02	5.43	0.78
1000	Born level	4.659	0.241	0.0235	2.229
	corrected	3.617	0.227	0.0276	2.184
	corrections/%	-22.36	-5.64	17.08	-2.05
2000	Born level	1.218	0.234	0.0220	2.307
	corrected	0.647	0.207	0.0321	2.168
	corrections/%	-46.86	-11.53	46.11	-6.02

Table 3: Lowest-order predictions and corresponding corrections for various observables and $|\cos\theta_{\text{cut}}| = 0.8$

M_W fixed	UUUU	++TT	++LL	+ -TT	+ -LL	+ -(LT + TL)
$\theta = 20^\circ$	0.15%	0.18%	0.46%	0.14%	0.53%	0.06%
$\theta = 90^\circ$	0.62%	0.58%	3.52%	0.44%	1.50%	0.29%
integrated over						
$10^\circ < \theta < 170^\circ$	0.22%	0.26%	1.06%	0.16%	1.23%	0.25%
$20^\circ < \theta < 160^\circ$	0.29%	0.33%	1.48%	0.21%	1.23%	0.26%

Table 4: Variation of various polarized cross-sections at $E_{\text{CMS}} = 500 \text{ GeV}$ for fixed M_W with the top-quark mass in the range $130 \text{ GeV} < m_t < 210 \text{ GeV}$ in per cent of the cross-section for $m_t = 174 \text{ GeV}$

dominates $\sigma_{\pm\pm\text{LL}}$ in an even wider range, we have omitted this cross-section in the tables for the Higgs dependence.

In Tables 4 and 5 the W-boson mass is kept fixed at $M_W = 80.22 \text{ GeV}$. Then, as argued in the previous section, the variation is small owing to the absence of large top- and Higgs-mass-dependent corrections. The larger variation of the cross-sections involving longitudinal W bosons is due to terms proportional to m_t^2/M_W^2 or M_H^2/M_W^2 arising as a remnant of the unitarity cancellations for $\sqrt{s} \gg m_t, M_H$. These terms induce a sizable variation of these cross-sections with m_t and M_W at higher energies.

The variations of the corrections for fixed G_μ are shown in Tables 6 and 7. It is larger in particular for the cross-sections for purely transverse W bosons. This fact results from the dependence of M_W on m_t and M_H that involves logarithmic top- and Higgs-mass-dependent terms and terms proportional to m_t^2/M_W^2 .

To visualize the Higgs resonance, we plot in Fig. 11 the cross-section including $\mathcal{O}(\alpha)$ corrections integrated over $20^\circ < \theta < 160^\circ$ for various values of the Higgs-boson mass.

M_W fixed	UUUU	++TT	+−TT	+−LL	+−(LT + TL)
$\theta = 20^\circ$	0.16%	0.18%	0.13%	0.37%	0.81%
$\theta = 90^\circ$	0.44%	0.21%	0.34%	2.62%	1.51%
integrated over					
$10^\circ < \theta < 170^\circ$	0.09%	0.12%	0.10%	2.04%	0.37%
$20^\circ < \theta < 160^\circ$	0.07%	0.09%	0.06%	2.06%	0.52%

Table 5: Variation of various polarized cross-sections at $E_{\text{CMS}} = 500$ GeV for fixed M_W with the Higgs-boson mass in the ranges $60 \text{ GeV} < M_H < 400 \text{ GeV}$ and $600 \text{ GeV} < M_H < 1000 \text{ GeV}$ in per cent of the cross-section for $M_H = 250$ GeV

G_μ fixed	UUUU	++TT	++LL	+−TT	+−LL	+−(LT + TL)
$\theta = 20^\circ$	1.20%	1.24%	1.39%	1.17%	0.45%	0.05%
$\theta = 90^\circ$	0.18%	0.06%	3.23%	0.20%	1.56%	1.22%
integrated over						
$10^\circ < \theta < 170^\circ$	0.98%	0.94%	1.62%	1.12%	1.17%	0.84%
$20^\circ < \theta < 160^\circ$	0.52%	0.51%	2.03%	0.67%	1.19%	0.95%

Table 6: Same as in Table 4 but now for fixed G_μ

Our results agree qualitatively⁴ well with those of Ref. [10]. While the resonance is comparably sharp at small energies, it is washed out by the large width of the Higgs boson at high energies. Already for $M_H = 400$ GeV the Higgs resonance is hardly visible in $\gamma\gamma \rightarrow W^+W^-$.

6 Summary

The process $\gamma\gamma \rightarrow W^+W^-$ will be one of the most interesting reactions at future $\gamma\gamma$ colliders. In particular, it is very useful to study triple and quartic non-Abelian gauge couplings.

⁴See footnote 3.

G_μ fixed	UUUU	++TT	+−TT	+−LL	+−(LT + TL)
$\theta = 20^\circ$	0.33%	0.33%	0.35%	0.73%	0.81%
$\theta = 90^\circ$	0.56%	0.36%	0.55%	2.63%	1.26%
integrated over					
$10^\circ < \theta < 170^\circ$	0.36%	0.34%	0.38%	2.09%	0.25%
$20^\circ < \theta < 160^\circ$	0.31%	0.27%	0.32%	2.10%	0.37%

Table 7: Same as in Table 5 but now for fixed G_μ

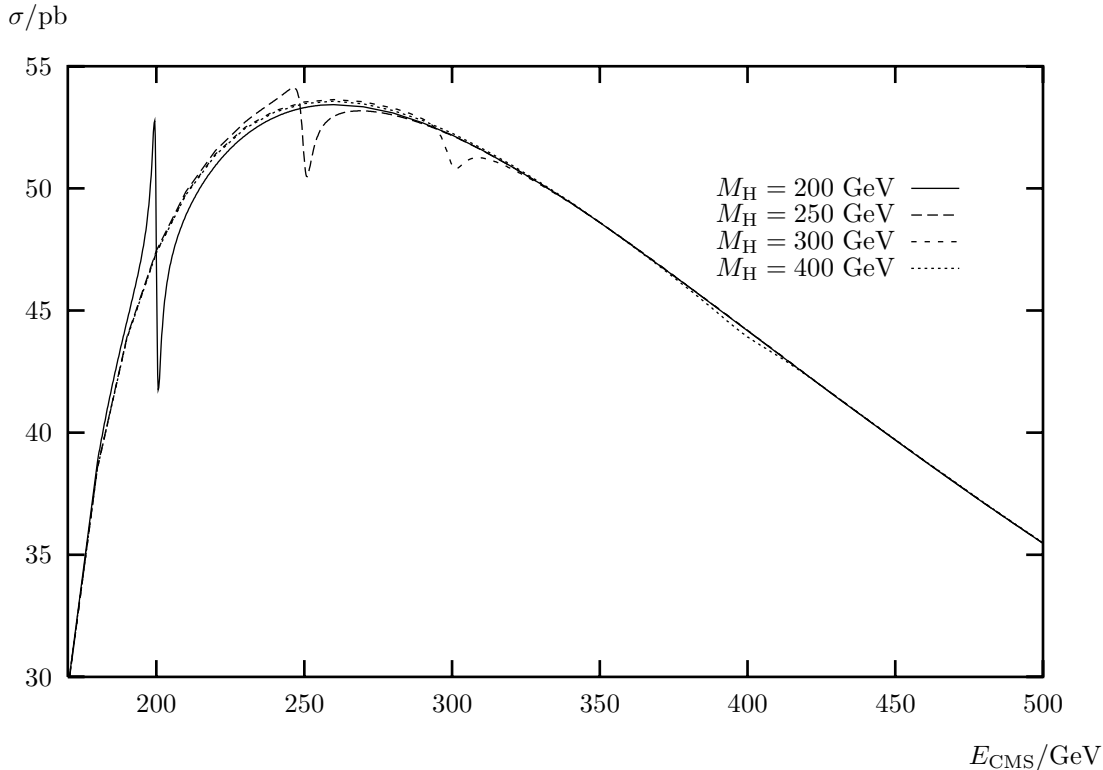


Figure 11: Integrated unpolarized cross-section including $\mathcal{O}(\alpha)$ corrections for various Higgs-boson masses ($20^\circ < \theta < 160^\circ$)

We have calculated the one-loop radiative corrections to $\gamma\gamma \rightarrow W^+W^-$ within the electroweak Standard Model in the soft-photon approximation for arbitrary polarizations of the photons and W bosons. By using a non-linear gauge-fixing term the number of contributing diagrams can be reduced by roughly a factor of two. An interesting peculiarity of $\gamma\gamma \rightarrow W^+W^-$ is the absence of most (universal) leading corrections, such as leading logarithms of light quark masses associated with the running of α and leading logarithms associated with collinear bremsstrahlung. Therefore, the theoretical predictions are very clean.

In the heavy mass limit no leading m_t^2 - and $\log m_t$ -terms and $\log M_H$ -terms exist. Consequently, the variation of the cross-sections with the top-quark and Higgs-boson masses is small if M_W is kept fixed with the exception of the cross-sections involving longitudinal W bosons at high energies. For fixed G_μ the variation arises mainly from the variation of M_W with m_t and M_H and is thus of similar origin like the one of $e^+e^- \rightarrow f\bar{f}$ or $e^+e^- \rightarrow W^+W^-$.

We have presented a detailed numerical discussion of the lowest-order cross-sections and the virtual and soft-photon corrections to $\gamma\gamma \rightarrow W^+W^-$. The soft-photon-cut-off-independent radiative corrections to the total cross-section are of the order of 10%. They are increased at high energies if the forward and backward regions are excluded by an angular cut. This is due to the fact that at high energies the radiative corrections reach

several 10% for intermediate scattering angles whereas they are at the level of several per cent in the forward and backward direction which dominate the total cross-section. The large corrections are caused by bosonic loop diagrams whereas the effects of the fermionic diagrams are of the order of 5–10%.

Acknowledgement

We are grateful to M. Böhm for useful discussions.

References

- [1] F. Abe et al., CDF collaboration, FERMILAB-PUB-95/022-E, hep-ex/9503002;
S. Abachi et al., DØ collaboration, FERMILAB-PUB-95/028-E, hep-ex/9503003.
- [2] F. Abe et al., CDF collaboration, FERMILAB-PUB-95/036-E, hep-ex/9503009.
- [3] I.F. Ginzburg, G.L. Kotkin, V.G. Serbo and V.I. Telnov, *Nucl. Instr. Meth.* **205** (1983) 47;
I.F. Ginzburg, G.L. Kotkin, S.L. Panfil, V.G. Serbo and V.I. Telnov, *Nucl. Instr. Meth.* **219** (1984) 5;
V.I. Telnov, *Nucl. Instr. Meth.* **A294** (1990) 72;
D.L. Borden, D.A. Bauer and D.O. Caldwell, SLAC-PUB-5715, 1992 (unpublished).
- [4] P.D. Pesic, *Phys. Rev.* **D8** (1973) 945;
I.F. Ginzburg, G.L. Kotkin, S.L. Panfil and V.G. Serbo, *Nucl. Phys.* **B228** (1983) 285,
E:Nucl. Phys. **B243** (1984) 550;
M. Katuya, *Phys. Lett.* **124B** (1983) 421.
- [5] K.J. Kim and Y.S. Tsai, *Phys. Rev.* **D8** (1973) 3109;
G. Tupper and M.A. Samuel, *Phys. Rev.* **D23** (1981) 1933;
S.Y. Choi and F. Schrempp, *Phys. Lett.* **B272** (1991) 149.
- [6] E. Yehudai, *Phys. Rev.* **D44** (1991) 3434.
- [7] G. Bélanger and F. Boudjema, *Phys. Lett.* **B288** (1992) 210.
- [8] M.A. Shifman, A.I. Vainshtein, M.B. Voloshin and V.I. Zakharov Shifman, *Sov. J. Nucl. Phys.* **30** (1979) 711.
- [9] E.E. Boos and G.V. Jikia, *Phys. Lett.* **B275** (1992) 164.
- [10] D.A. Morris, T.N. Truong and D. Zappalá, *Phys. Lett.* **B323** (1994) 421.
- [11] H. Veltman, *Z. Phys.* **C62** (1994) 235.
- [12] A. Denner, S. Dittmaier and R. Schuster, Bielefeld preprint BI-TP 94/51, Würzburg preprint UWITP 94/04, hep-ph/9411268, to appear in *Phys. Rev.* **D**.
- [13] S. Wolfram, *Mathematica — A System for Doing Mathematics by Computer* (Addison-Wesley, Redwood City, CA, 1988).
- [14] J. Küblbeck, M. Böhm and A. Denner, *Comp. Phys. Commun.* **60** (1990) 165;
H. Eck and J. Küblbeck, *Guide to FeynArts 1.0*, University of Würzburg, 1992.

- [15] R. Mertig, M. Böhm and A. Denner, *Comp. Phys. Commun.* **64** (1991) 345;
R. Mertig, *Guide to FeynCalc 1.0*, University of Würzburg, 1992.
- [16] K. Fujikawa, *Phys. Rev.* **D7** (1973) 393;
M. Bacé and N.D. Hari Dass, *Ann. Phys.* **94** (1975) 349;
B.W. Lee and R.E. Shrock, *Phys. Rev.* **D16** (1977) 1444;
M.B. Gavela, G. Girardi, C. Mallevalle and P. Sorba, *Nucl. Phys.* **B193** (1981) 257;
N.G. Deshpande and M. Nazerimonfared, *Nucl. Phys.* **B213** (1983) 390;
F. Boudjema, *Phys. Lett.* **B187** (1987) 362.
- [17] A. Denner, *Fortschr. Phys.* **41** (1993) 307;
M. Böhm and A. Denner, *Radiative Corrections in the Electroweak Standard Model*,
in *Proceedings of the Workshop on High Energy Phenomenology*, Mexico City, 1991,
eds. R. Huerta and M.A. Perez (World Scientific, Singapore, 1992), p. 1.
- [18] G. 't Hooft and M. Veltman, *Nucl. Phys.* **B153** (1979) 365;
W. Beenakker and A. Denner, *Nucl. Phys.* **B338** (1990) 349;
A. Denner, U. Nierste and R. Scharf, *Nucl. Phys.* **B367** (1991) 637.
- [19] C.N. Yang, *Phys. Rev.* **77** (1950) 242.
- [20] E. Braaten and J.P. Leveille, *Phys. Rev.* **D22** (1980) 715;
M. Drees and K. Hikasa, *Phys. Lett.* **B240** (1990) 455, *E:Phys. Lett.* **B262** (1991)
497;
J. Fleischer and F. Jegerlehner, *Phys. Rev.* **D23** (1981) 2001;
D.Yu. Bardin, P.Kh. Khristova and B.M. Vilenskii, *Sov. J. Nucl. Phys.* **53** (1991)
152 and Dubna preprint JINR-P2-91-140;
B.A. Kniehl, *Nucl. Phys.* **B352** (1991) 1, *Nucl. Phys.* **357** (1991) 439 and *Nucl. Phys.*
376 (1992) 3;
A. Dabelstein and W. Hollik, *Z. Phys.* **C53** (1992) 507.
- [21] W. Beenakker et al., *Nucl. Phys.* **B410** (1993) 245 and *Phys. Lett.* **B317** (1993) 622.
- [22] D. Bardin, W. Beenakker and A. Denner, *Phys. Lett.* **B317** (1994) 213;
V.S. Fadin, V.A. Khoze and A.D. Martin, Durham preprint DTP/94/116, hep-
ph/9501214.
- [23] G. Passarino and M. Veltman, *Nucl. Phys.* **B160** (1979) 151.
- [24] Particle Data Group, *Phys. Rev.* **D50** (1994) 1173.
- [25] M.L. Swartz, preprint SLAC-PUB-6710, 1994, hep-ph/9411353;
A.D. Martin and D. Zeppenfeld, preprint MAD/PH/855, 1994, hep-ph/9411377;
S. Eidelman and F. Jegerlehner, preprint PSI-PR-95-01, BudkerINP 95-5, hep-
ph/9502298.
- [26] W. Beenakker and A. Denner, *Int. J. Mod. Phys.* **A9** (1994) 4837.